1   **Strain localized deformation variation of a small-scale ductile shear zone**

2   Lefan Zhan[1], Shuyun Cao*[1], Yanlong Dong[1], Wenyuan Li[1]

3   [1]State Key Laboratory of Geological Processes and Mineral Resources, China University

4   of Geosciences, Wuhan 430074, China

5   **Correspondence:** Shuyun Cao (Shuyun.cao@cug.edu.cn)

6   **Abstract:**

7   A continental-scale strike-slip shear zone frequently presents a long-lasting

8   deformation and physical expression of strain localization in a middle to lower crustal

9   level. However, the deformation evolution of strain localization at a small-scale shear

10   zone remains unclear. This study investigated <10 cm wide shear zones developing in

11   undeformed granodiorites exposed at the boundary of the continental-scale Gaoligong

12   strike-slip shear zone. The small-scale ductile shear zone demonstrated a typical

13   transition from protomylonite, mylonite to extremely deformed ultramylonite, and

14   decreased mineral size from coarse-grained aggregates to extremely fine-grained mixed

15   phase. Shearing senses such as hornblende and feldspar porphyroclasts in the shear zone

16   are the more significantly low-strain zone of mylonite. The microstructure and EBSD

17   results revealed that the small-scale shear zone experienced ductile deformation under

18   medium-high temperature conditions. Quartz aggregates suggested a consistent

19   temperature with an irregular feature, exhibiting a dominated high-temperature prism

20   <a>slip system. Additionally, coarse-grained aggregates in the mylonite of the shear zone

21   were deformed predominantly by dislocation creep, while ultra-plastic flow by viscous

22   grain boundary sliding was an essential deformation process in the extremely fine-

23   grained (~50μm) mixed-phase of ultramylonite. Microstructural-derived strain rates

24   calculated from quartz paleopiezometry were on the order of 10^{-15} to 10^{-13} s^{-1} from low-

25   strain mylonite to high strained ultramylonite. The localization and strain rate-limited

26   process was fluid-assisted precipitation presenting transitions of compositions as

27   hydrous retrogression of hornblende to mica during increasing deformation and

28   exhumation. Furthermore, the potential occurrence of the small-scale shear zone was

29   initiated at a deep-seated crustal dominated by the temperature-controlled formation and

30   rheological weakening.

31   **Keywords:** strain localization, ductile deformation, ultramylonite, microstructure,

32   EBSD texture, Gaoligong shear zone

34   **1. Introduction**

35   Many previous studies (e.g., field analysis, laboratory experiments, numerical

36 modeling, seismology, hydrogeology) have focused on describing and discussing the
37 architecture, initiation mechanisms, and rock failure processes of the shear zone (Sibson,
38 1977; Scholz, 1980, 1989; Wintsch et al., 1995; Tikoff and de Saint Blanquat, 1997;
39 Brown and Solar, 1998; Rosenberg, 2004; Mancktelow, 2008; Wibberley et al., 2008;
40 Frost et al., 2011; Mancktelow and Pennacchioni, 2013; Cao and Neubauer, 2016; Fossen
41 and Cavalcante, 2017; Menegon et al., 2017; Vannucchi, 2019; Fagereng and Beall,
42 2021). The shear zone is known that strain localizes into the tabular zone from small
43 outcrop-size individual zone to large composite structure in the large-scale in the
44 lithosphere (Fossen and Cavalcante, 2017). The continental-scale strike-slip shear zone
45 commonly appears as long-standing zones of weakness in the crust, which extend across
46 ductile lower crust (shear zone) through the brittle-ductile transition into brittle crust
47 (fault zone) (Sibson, 1977; Scholz, 1980, 1989). The exhumed strike-slip shear zones at
48 depth are crucial structural borders within or between major continental blocks
49 influenced by lateral extrusion, recording the strain localization and regional kinematic
50 history (Ratschbacher et al., 1991; Cunningham and Mann, 2007; Cao and Neubauer,
51 2016). Besides, nucleation and initiation of a continental-scale shear zone occur within
52 the deep crust or even mantle lithosphere in a specific thermal-structural architecture,
53 where temperature-controlled rheological weakening plays a critical role in localizing
54 future strike-slip shear zone (Cao and Neubauer, 2016 and references therein). Although
55 numerous studies have established the small-scale (10^{-3}–10^{-1}m thick) ductile shear
56 zones within massive host rocks, the distribution and significance of shear localization
57 at small scales are controversial (e.g., Bons and Jessell, 1999; Mancktelow and
58 Pennacchioni, 2005, 2020; Pennacchioni, 2005; Menegon and Pennacchioni, 2009;
59 Pennacchioni and Zucchi, 2013; Pennacchioni and Mancktelow, 2018; Ceccato et al.,
60 2020).

61 Experiments and models on the deformation of rocks have been proposed to explain
62 the formation of shear zones in varied scales, including the lithosphere's strength, the
63 external conditions such as temperature, pressure, and fluid content, and the fact that
64 rocks' rheology depends on their composition and grain size (e.g., Evans, 2000; Faulkner
65 and Rutter, 2001; Collettini et al., 2009; Bense et al., 2013; Cao and Neubauer, 2016;
66 Fossen and Cavalcante, 2017; Liu, 2017). It is suggested that the small individual zones
67 can grow into the large and composite shear zone networks by segment linkage as they
68 accumulate strain and displacement (Pennacchioni, 2005; Vauchez et al., 2007; Ganade
69 de Araujo et al., 2014; Fossen and Cavalcante, 2017). The case from the field-based study
70 is inconsistent with argues the nucleation model of the shear zone by strain localization
71 in a homogeneous rheological media based on random distributions of weak particles or
72 through the dilation of the wing veins on either the compressed or extensional side
73 (Mancktelow, 2002, 2008; Misra and Mandal, 2007; Wehrens et al., 2016; Nevitt and

74 Pollard, 2017; Nevitt et al., 2017; Pennacchioni and Mancktelow, 2018). Besides, the
75 initial composition changes with fluid infiltration along and diffusion away from the
76 discontinuities as pre-existing brittle fractures, bringing high significance to the types of
77 developing shear zone (Mancktelow and Pennacchioni, 2005; Pennacchioni, 2005;
78 Pennacchioni and Zucchi, 2013; Pennacchioni and Mancktelow, 2018). However,
79 ongoing deformation and metamorphism can obliterate or reset any traces of such small-
80 scale localization (Bons and Jessell, 1999). Therefore, the processes and mechanism of
81 localizing in a small-scale shear zone are still unclear.

82   This study presents a detailed description of small-scale shear zones developing in
83 unfoliated large intrusive granodiorite bodies at the boundary of the Gaoligong
84 continental-scale shear zone (GLG-SZ) on the southeastern margin of the Tibetan Plateau.
85 The new detail microstructural, EBSD texture, and geothermal data reveal that (1) strain
86 localization in small-scale shear zones is characterized by the development of mylonite
87 and ultramylonite with the increasing strain from rim to the center, (2) formation
88 conditions and processes of the micro-shear zone are associated with the continental-
89 scale GLG-SZ ductile shearing and exhumation.

2. Geological setting and field description

91   The southeastern margin of the Tibetan Plateau has been engaged in crustal
92 thickening, tectonic compression, block rotation, and strike-slip shearing during the
93 Cenozoic (Tapponnier and Molnar, 1977; Tapponnier et al., 1982, 1990) (Fig. 1). Several
94 continental-scale strike-slip shear zones including the Gaoligong shear zone (GLG-SZ),
95 the Chongshan-Biluoxueshan shear zone, and the Ailaoshan-Red River shear zone are
96 developed in the Sanjiang region (Jinshajiang, Lancangjiang, and Nujiang) (Fig. 1). The
97 formation of these strike-slip shear zones has been attributed to the Cenozoic continental
98 collision of the India and Eurasia plates. The GLG-SZ is a narrow N-S trending belt with
99 a width of 10 kilometers and a length of 600 kilometers, extending southward from the
100 eastern Himalayan Syntaxis to the eastern Tengchong area and then extending
101 southwestward to join the Sagaing fault zone (Fig. 1B). It serves as the boundary between
102 the Tengchong and Baoshan blocks (Ji et al., 2000a; Zhang et al., 2012a, b; Liu et al.,
103 2017; Dong et al., 2019; Tang et al., 2020). The Cambrian gneiss and the Neoproterozoic
104 metamorphic units, named the Gaoligong metamorphic complex, represent the basement
105 units in this area and evolve into the Gaoligong strike-slip shear zone along after the
106 reactivation in Cenozoic (Wang et al., 2006; Wang et al., 2008; Zhang et al., 2012b; Zhu
107 et al., 2017; Dong et al., 2019) (Fig. 1B). The main rock types are mylonitic gneisses
108 (granitic gneisses and migmatitic gneisses) and schists, as well as amphibolites and
109 marbles.

110   Along the GLG-SZ, a considerable number of Mesozoic and Cenozoic granitic
111 rocks intrude into the Gaoligong metamorphic complex (Wang et al., 2006; Zhang et al.,

112   2018; Dong et al., 2019) (Fig. 1B). Recent zircon U-Pb and ^{39}Ar/^{40}Ar chronological data
113   revealed that both of the unfoliated and foliated granitic intrusions in the northwest part
114   of the GLG-SZ has the emplaced ages of 112–125 Ma (Early Cretaceous) during the
115   collision of the Lhasa and the Qiangtang blocks, post-magmatic melting timing of ca. 35
116   Ma (Early Oligocene), and subsequent cooling during the Middle Miocene (ca. 13 Ma)
117   (Xu et al., 2012; Zhu et al., 2017; Dong et al., 2021). Two-stage tectono-thermal
118   evolutions since the Late Cretaceous have also been proposed. Around 76–74 Ma, earlier
119   regional metamorphism occurs in the high-pressure granulite facies owing to crustal
120   thickening and magmatism. Around 24–23 Ma, the later stage was defined by
121   amphibolite-greenschist facies conditions in connection with shearing deformation (Ji et
122   al., 2000b; Song et al., 2010). The analysis of geochronological data from the Tengchong
123   area suggests that the dome uplift and deep crustal material was exhumed during 32–10
124   Ma in the south of the GLG-SZ (Xu et al., 2015; Zhang et al., 2017; Dong et al., 2019).
125   Within the GLG-SZ, the high-grade rocks and most of the granitic intrusions within
126   the GLG-SZ underwent the Cenozoic deformation of right-lateral strike-slip shear
127   (Zhang et al., 2012b; Xu et al., 2015; Liu et al., 2017; Chiu et al., 2018; Dong et al., 2019)
128   (Fig. 2A, B). The rocks demonstrate dominated characteristics of ductile deformation
129   structures, including asymmetric folds, highly developed mylonitic lineation, fine-
130   grained minerals, S-C fabrics, and shear bands (Dong et al., 2019). All shear sense
131   indicators of σ- and δ-porphyroclasts (Figs. 2A, B), as well as S-C fabrics and
132   asymmetric folds, exhibit strong dextral shear. Mylonites are characterized with L>>S-
133   type structures, in which the mineral stretching lineation is far more developed than
134   mylonitic foliation (Fig. 2B). The foliation runs approximate N-S trending and dips
135   moderately to steeply to the east (27–78°), while the lineation slightly dips to the north
136   or south (<23°) (Fig. 1C; Dong et al., 2019).
137   This study emphasizes the small-scale shear zones newly observed within the
138   unfoliated granidiorite at the western part of the GLG-SZ. The magmatic fabric of
139   granidiorite is deficient in solid-state ductile deformation features and presents randomly
140   arranged feldspar phenocrysts (Fig. 2). The small-scale shear zones have a thickness of
141   approximately 10^{-3}–10^{-1}m. Most structures are steeply dipping, and the orientations are
142   relatively disorderly (Fig. 1C).

143
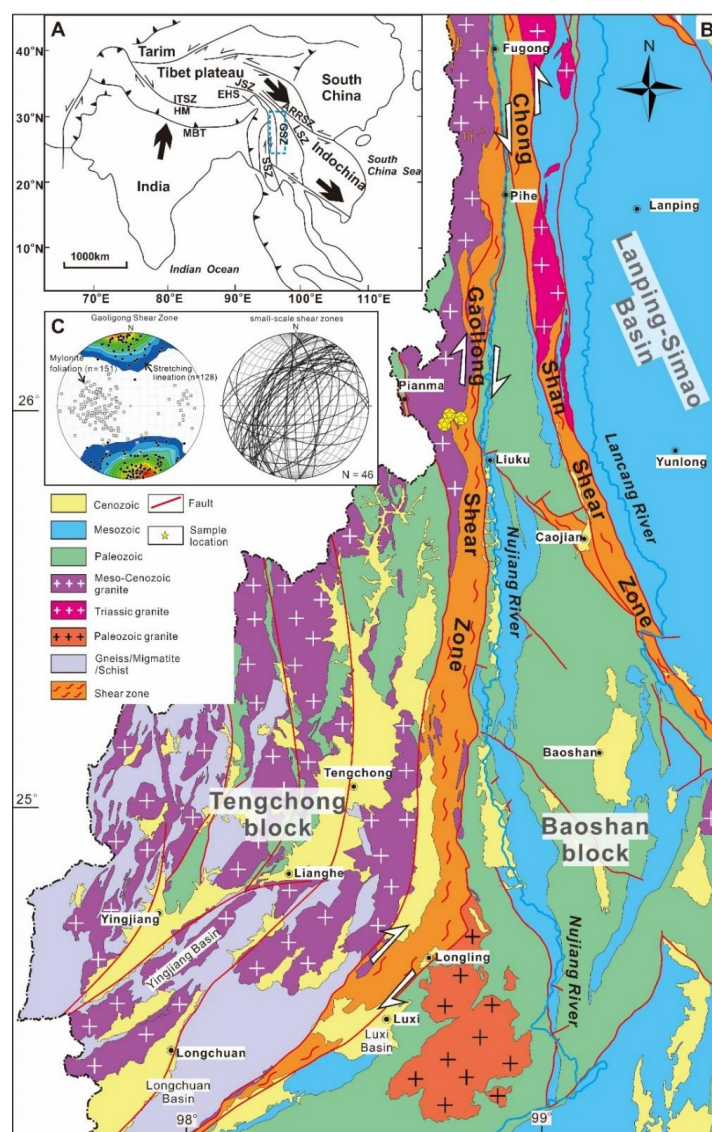
Fig.1. The Geological maps of the San Jiang region and the Gaoligong shear zone. (A)
Regional tectonic map of the India-Eurasian plate. (B) Simplified geological map of the
San Jiang region modified from Wang et al., 2008 and Dong et al., 2021; (C) Foliation
and lineation data for GLG-SZ and the strikings of small-scale shear zones, plotted in
stereographic projection (lower hemisphere). ARRSZ: Ailaoshan-Red River Shear Zone;
EHS: Eastern Himalayan Syntaxis; GLG-SZ: Gaoligong shear zone; CSZ: Chongshan
Shear Zone; JSZ: Jiali Shear Zone; SF: Sagaing fault.

3. Analytical methods

3.1 Microscopy and cathodoluminescence

Microstructure and petrology in the small-scale shear zone and granidiorite rock were investigated in thin sections by optical and SEM, cathodoluminescence (CL) imaging, and electron backscatter diffraction (EBSD). A Sigma 300VP field emission scanning electron microscope (FEG-SEM) and BII CLF-2 Cathodoluminescence (CL) are employed in the China University of Geosciences (Wuhan). CL operated at a voltage of 15KV, power consumption of 150 W, a current of 300 A, and a beam current of 1 mA with a diameter of 30 μm.

3.2 Electron backscatter diffraction (EBSD)

The Sigma 300VP FEG-SEM with a Symmetry EBSD (electron backscatter diffraction) detector in China University of Geosciences (Wuhan) was applied to obtain the mineral CPO. The highly polished thin sections with conductive tape attached to the surface were put in the SEM chamber and rotated at a 70° tilt angle. Electron backscatter patterns were acquired using the automatic mapping mode under the conditions of low vacuum, with a detector distance of 193.1 mm, an acceleration voltage of 20 kV, and a beam working distance of 15.6 mm. Indexing is considered acceptable when at least six detected kikuchi bands correspond to those in the analyzed mineral phases' standard reflector file. Following the completion of the test, the electron backscatter pattern analysis was performed using the Aztec Crystal and HKL Channel 5. The pole figure of representative CPO in samples was plotted in equal-area stereographic diagrams using the lower hemisphere projection and the base circle represents the X-Z plane parallel to the lineation and vertical to the foliation. Automated orientation maps revealed systematic not-indexing, and such data were replaced with zero solution pixels.

3.3 EPMA methodology

Compositional data of unfoliated granitoids and foliated granitic rocks were measured on a JEOL electron microprobe (JXA-8600) with a wavelength dispersive system at the Department of Geography and Geology, University of Salzburg. Measuring conditions using a focused electron beam involved a 15 kV acceleration voltage and a 40 nA sample current. The calibration of the microprobe was performed based on natural silicates and synthetic oxides standards. The matrix correction for quantitative analysis was conducted by the ZAF oxide method for most silicate minerals. The detection limits (2σ) are 0.06 wt% and 0.04 wt% for Si and Al, respectively, and are 0.025 wt% for Na, K, Mg, Mn, and Fe.

4. Deformed characteristics of granodiorites and small-scale shear zones

4.1 Mesoscale structures of granodiorites and small-scale shear zones

As mentioned above, the GLG-SZ exposed widespread granitic intrusions of various ages (Fig. 1B) (Zhang et al., 2017; Zhu et al., 2017; Chiu et al., 2018; Zhang et

190 al., 2018; Tang et al., 2020; Dong et al., 2021). Most granitic intrusions underwent strong
191 mylonitization within the GLG-SZ. Notably, the unfoliated granodiorites were exposed
192 at the western boundary of the GLG-SZ. The major body of the studied granodiorites
193 exhibits little macroscopic evidence of solid-state deformation-metamorphism, and
194 igneous relationships are well preserved (Fig. 2C-H).

195 The granodiorites present strain localization on a network of different types of
196 small-scale shear zones with a thickness of approximately 10^{-3}–10^{-1} m. They are
197 invariably localized on approximately planar structural and compositional
198 heterogeneities within the protolith (Fig.2C, D). The small-scale shear zones exhibit
199 significant ductile and/or brittle deformation characteristics. Regarding centimeter-scale
200 or decimeter-scale shear zones, the strain is strongly localized in a narrow band, and
201 minerals are elongated directionally in the outcrop scale (Fig.2C, D). Most structural and
202 compositional heterogeneities demonstrate a nearly horizontal stretching lineation and
203 extremely fine-grained minerals of ductile shearing. The enclaves occur in the
204 granodiorites crosscut by isolated, knife-sharp (<1–3 mm wide) brittle fractures, and may
205 have a strike length of many tens of meters (Fig. 2G). The brittle fractures are typically
206 identified by a dark biotite-rich slit. Most of these reflect displacement discontinuities in
207 the outcrop scale. For example, cross-cut markers (e.g., mafic enclaves) are severely
208 truncated and displaced by the shear zones without any dragging effect (Fig. 2G, H).
209 Some display bands and several centimeters wide of a sigmoidal-shaped foliation of
210 ductile shearing, implying a dextral sense of shear (Fig. 2F, H).

211
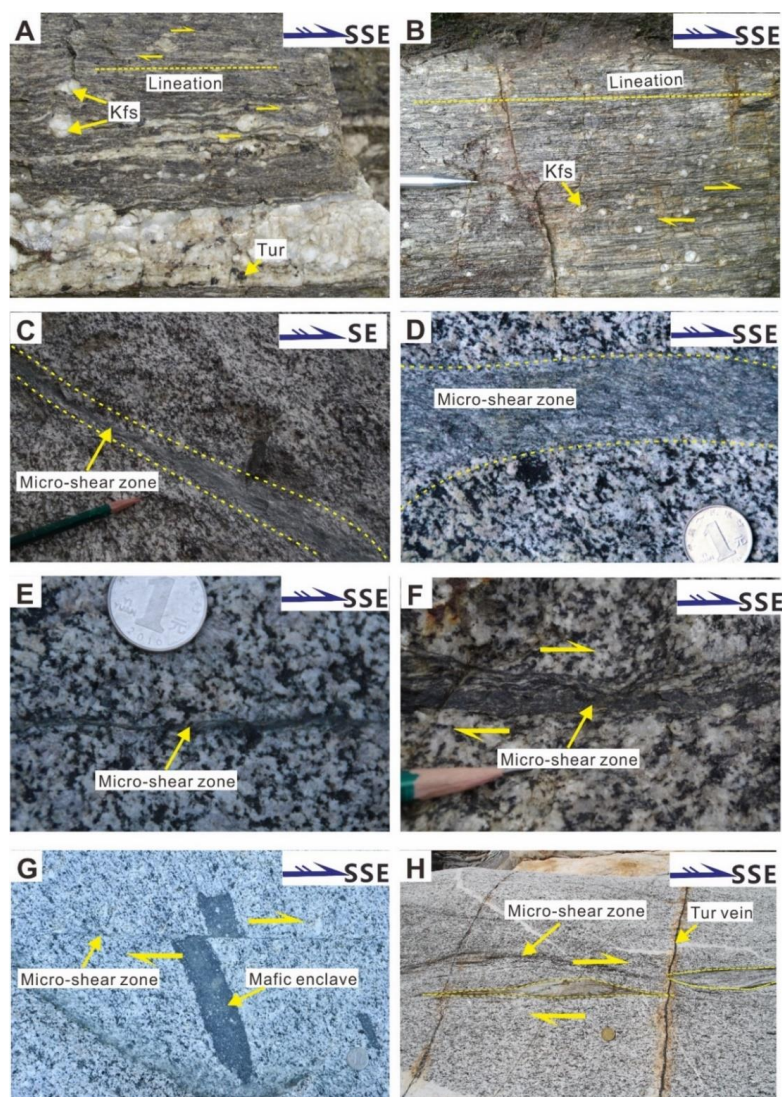
Fig.2. Field structures of the GLG-SZ and small-scale shear zones. (A)-(B) Some
representative deformation structures of the GLG-SZ in the XZ plane (the plane parallel
to the lineation and vertical to the foliation). (C)-(D) Ductile shear zones in the
centimeter-scale/ decimeter-scale. (E) millimeter-scale ductile shear zones are like joints
in the outcrop scale. (F) millimeter-scale shear zones form a sigmoidal-shaped foliation
at the shear zone boundaries. (G)-(H) Dextral offset of some crosscut markers across
millimeter-scale shear zones.

219

4.2 Microstructures of unfoliated granodiorite

The unfoliated granodioritic host rocks are composed of quartz (16–19 vol%), K-feldspar (17–19 vol%), plagioclase (~59–63 vol%), hornblende (~7 vol%), and biotite (2-3 vol%). The unfoliated granodioritic exhibits little evidence of ductile deformation. Feldspar and hornblende grains both primarily consist of euhedral to subhedral coarse grains and form with microfracture (Fig. 3A). The coarse-grained feldspar grains are dominated by plagioclase and tiny amounts of K-feldspar. The plagioclase (up to several millimeters in length) has significant polysynthetic twinning and ring or zoning magma structure that grows fine-grained inclusions of biotite and quartz grains (Fig. 3A). The crystal sizes of hornblende are about 0.5–5 mm, and the grains develop two groups of cleavages (Fig. 3B). Quartz grains present polycrystal aggregates, which are mostly xenomorphic around the plagioclase grains. The biotite grains demonstrate the features of an undeformed or only slightly bent shape with magmatic phase (Fig. 3C).

4.3 Microstructures of the small-scale shear zone

Under the microscope, the small-scale shear zone developing in the granodiorite has dramatical shearing banding, reflecting a transition deformation characteristic from protolith to ultramylonite. The mineral grain size gradually decreases from rim to center, with a strong strain gradient. According to the different grains size, three distinct deformed microstructure zones can be recognized (Fig. 3): Zone A with relatively close to the outer/rim low strain portions (Fig. 3D), high fine-grained Zone B of traversing into the shear zones, and strong fine-grained Zone C in the center of the shear zone.

Zone A in the small-scale shear zone is of the rim outer relative low strain portions, composed of plagioclase, K-feldspar, biotite, quartz, and a small amount of apatite. It presents the characteristics of protomylonite. The coarse-grained plagioclase, K-feldspar, and hornblende are well preserved. The fine-grained quartz grains form polycrystal aggregate ribbons. The borders of quartz grains exhibit various morphologies, ranging from slightly curved to serrated (Fig. 3C), suggesting characteristics of dynamic recrystallization by grain boundary migration (GBM). The large plagioclase grains develop mechanical twins and fractures locally. Some of the fractures of plagioclase crosscutting the grains are filled by quartz (Fig. 3C).
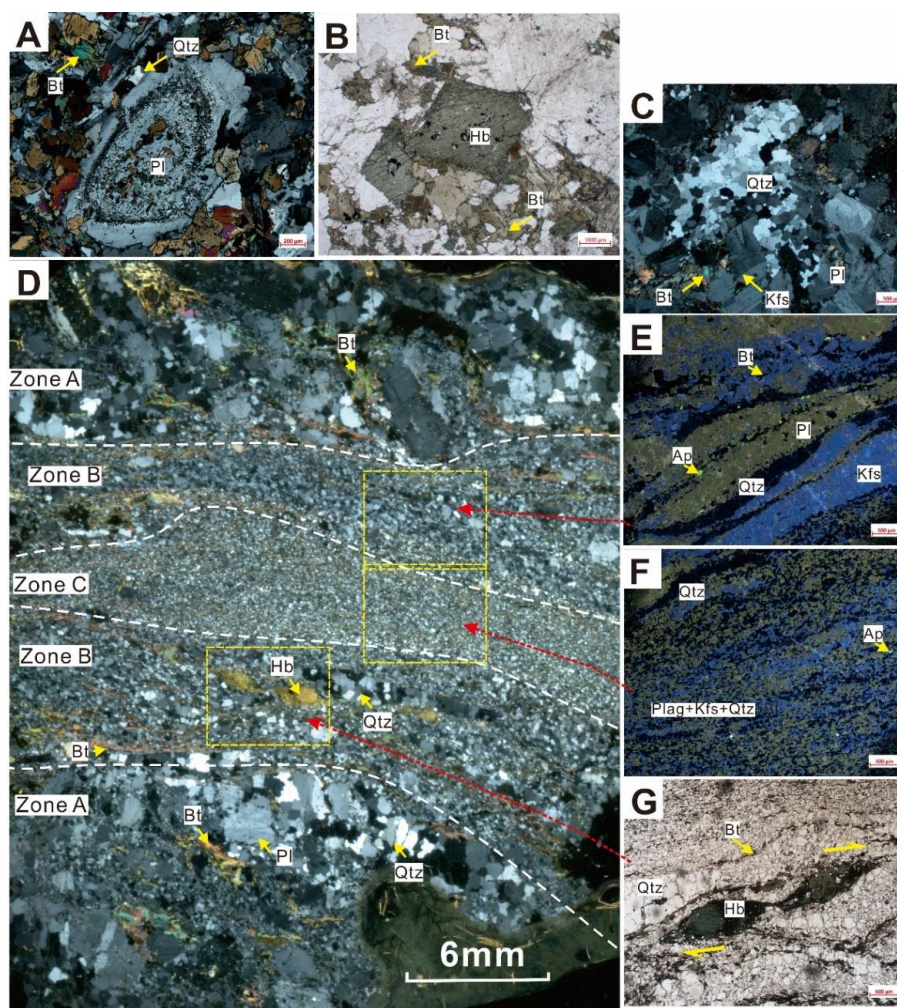
Fig.3. *Microscopic deformation characteristics of unfoliated granodiorite and small-scale shear zones. (A) Ring or zoned structure of plagioclase in the unfoliated granodiorite. (B) The euhedral to subhedral hornblende crystals in the unfoliated granodiorite s. (C) quartz-rich aggregates and feldspar porphyroclast with mechanical twinning and fractures in the Zone A of shear zone. (D) Thin section scanning of small-scale shear zone. (E) Fine-grained layers in the Zone B. (F) The mixed-phase zone in the Zone C of shear zone. (G) The residual hornblende grains indicating right-lateral shearing in the Zone B of shear zone. Fig. (B), (G) are plane polarized light micrographs, (A), (C) and (D) are cross-polarized light micrographs and (E), (F) are cathodoluminescence (CL) images. Qtz: quartz, Pl: plagioclase, Kfs: K-feldspar, Bt: biotite, Hb: hornblende, Ap: apatite.*

263   Under the SEM observation, the BSE images reveal a characteristic core-mantle
264 structure in the K-feldspar porphyroclasts surrounded by fine grains or subgrains (Fig.
265 4A, average length 760 μm). The long axes of porphyroclasts are parallel or oblique to
266 the shear zone. Myrmekites develop at the rim of the K-feldspar porphyroclasts.
267 Neocrystallization quartz grains (average length 45 μm, Fig 4B) within myrmekites are
268 elongated vertical to the long axis of K-feldspar porphyroclasts. Neocrystallization
269 plagioclase grains (average length of ~60 μm) within the myrmekites are equiaxed. The
270 fine-grained quartz and plagioclase grains nucleate around K-feldspar porphyroclasts
271 (Fig. 4A, B). The mica grains (average length 10 μm) are long-prismatic and plate-
272 prismatic, slenderer than these in the main body of granodiorite (Fig. 3C, D). Several
273 mica pieces are parallel to each other, and they cut across quartz aggregates or locate in
274 the edge of aggregates (Fig. 3C, D). Some newly formed micas precipitate in the
275 fractures of plagioclase grains and the grain boundaries of quartz aggregates (Fig. 3D).

276   The deformed Zone B is the most prominent characteristic of the mylonites with
277 the porphyroclasts (feldspar and hornblende) embedded in a fine-grained matrix (Fig.
278 3D, E). The feldspar porphyroclasts are smaller in size compared to Zone A, with the
279 features of elongated and lenticular, as well as irregular and serrated grain boundaries.
280 Inhomogeneous extinctions of porphyroclastic feldspar grains are apparent, indicating
281 plastic deformation. The elongated hornblende porphyroclasts form the mineral fish
282 fabrics, presenting a dextral sense of shear (Fig. 3D, G). Locally, the quartz grains form
283 typical polygonal aggregates, with the long axis parallel to or subparallel to the major
284 stretching lineation in the small-scale shear zone. The matrix consists of plagioclase, K-
285 feldspar, quartz, and biotite, containing a minor content of apatite. The mineral phases in
286 the fine-grained matrix are not homogeneously mixed. Instead, the layering of
287 compositions can be observed (Fig. 3E). Those layered aggregates of minerals exhibit an
288 orientation roughly parallel to the mylonitic foliation.

289   The BSE images imply that the K-feldspar layers are composed of many small
290 aggregates of fine-grained quartz and plagioclase (Fig. 4D, E). The same situation can
291 be observed in the plagioclase layers (Fig. 4D, F). Additionally, some small grains of
292 mica are distributed in the plagioclase grain boundaries as rod-like cross-sections (Fig.
293 4F). In contrast to the quartz-rich aggregates in Zone A, the quartz aggregates in Zone B
294 are not bulk but layered (Fig. 3E). The grain boundary of quartz is irregular. Moreover,
295 many relatively small, recrystallized quartz grains are mixed with K-feldspar, plagioclase,
296 and biotite in the matrix at the edge of the aggregates (Fig. 4D). In the quartz-rich layers,
297 isolated K-feldspar grains exist at triple junctions of quartz grains, and some small grains
298 of biotite are distributed in the grain boundary (Fig. 4D). Except for the small grains in
299 the quartz grain boundary, most biotite grains are highly elongated subparallel to the
300 foliation and form biotite-rich layers (Fig. 3G).
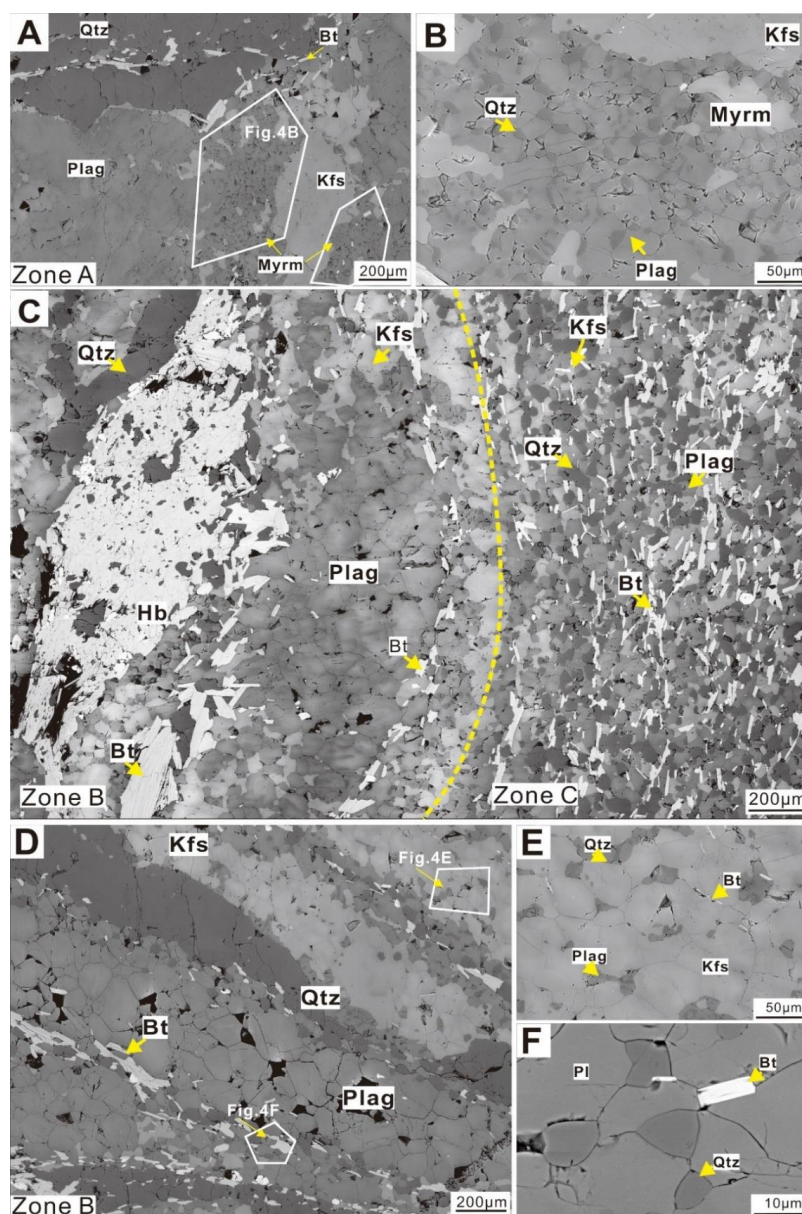
Fig.4. SEM-BSE images of small-scale shear zone. (A)-(B) Quartz and Plagioclase
irregular aggregates and the nucleation of fine-grained quartz and plagioclase grains
around K-feldspar clasts in the Zone A. (C) The transition area from Zone B to Zone C.
(D) Fine-grained layers in the Zone B. (E) The nucleation of fine-grained quartz and
plagioclase grains in K-feldspar-rich layers in the Zone B. (F) The nucleation of fine-
grained quartz in plagioclase -rich layers in the Zone B.

309   Zone C presents the dominated characteristics of ultramylonites composed of
310 extreme fine-grained matrix and only a few feldspar porphyroclasts with irregular grain
311 boundaries. The hornblende disappears. Zone C is microstructurally more homogeneous
312 than the other two zones and consists of fine-grained K-feldspar and plagioclase grains
313 (Fig. 3D, F). The fine-grained grains of feldspar, quartz, and mica are slightly elongate
314 or sub-equant. The feldspar porphyroclasts have disappeared. Quartz grains are
315 disseminated throughout the matrix, and the residual quartz-quartz grain boundaries are
316 more straight compared with those in the quartz aggregates in Zone A or Zone B (Fig.
317 4C). Phase boundaries between quartz and plagioclase or K-feldspar are frequently
318 extensively curved. The biotite grains distribute homogeneously in the matrix and are
319 extremely elongated subparallel to the foliation (Fig. 3F, 4C).

4.4 Mineral grain sizes of the small-scale shear zone

321   The grain size significantly decreases as the strain increases from Zone A to Zone C.
322 The software Image J is adopted to count the size of grains by manual operation.
323   In Zone A, the quartz grain sizes in the quartz-rich aggregates are counted. The mean
324 and median grain sizes are 186 μm and 173 μm, respectively (Fig. 5B, C). In Zone B,
325 the mean and median grain sizes are 88 μm and 80 μm, respectively (Fig. 5B, C). In the
326 weakly deformed domains (Zone A), a relatively broad distribution of grain size can be
327 observed, while a rather narrow distribution of grain size is observed in Zone B, (Fig.
328 5C). In Zone A and Zone B, larger grain sizes correspond to the grains without
329 recrystallization or recrystallization relict in the quartz-rich aggregates, and the smaller
330 grain sizes correspond to the small, neocrystallized quartz grains in the quartz-rich
331 aggregates or matrix at the edge of the aggregates. In Zone C, the mean diameter of
332 quartz grains is reduced to 44 μm, and it has the narrowest distribution among the three
333 zones (Fig. 5B, C).
334   The distribution of plagioclase grain size has a wide range from 80 to 1000 in Zone
335 A (Fig. 5C). The mean and median values of plagioclase grain size are 225 μm and 169
336 μm, respectively (Fig. 5B, C). In the box plot, the outliers represent large feldspar
337 porphyroclasts. Therefore, a considerable amount of plagioclase porphyroclasts occurs
338 in Zone A (Fig. 5C). In Zone B, the plagioclase grain size decreases dramatically. The
339 mean and median values of plagioclase grain size are 103 μm and 101 μm in Zone B,
340 respectively (Fig. 5B, C). The distribution of plagioclase grain size in Zone B is much
341 narrower than the distribution of plagioclase grain size in Zone A. The outliers in the box
342 plot suggest that the amount of plagioclase porphyroclasts significantly decreases in
343 Zone B (Fig. 5C). In Zone C, the mean and median diameters of plagioclase grains are
344 reduced to 65 μm and 63 μm, respectively. Meanwhile, it has the narrowest distribution
345 in the three zones, and there are hardly any plagioclase porphyroclasts (Fig. 5B, C).
346   Generally, the feldspar grain size is larger than the quartz grain size in all three

347   zones. The mean and median values of K-feldspar grain size are 165 μm and is 145 μm

348   in Zone A, respectively (Fig. 5B, C). The distribution of K-feldspar grain size is similar

349   to the distribution of quartz grain size in Zone A. In Zone B, the mean and median values

350   of K-feldspar grain size are all 97 μm. The distribution of K-feldspar grain size in Zone

351   B is narrower than the distribution of K-feldspar grain size in Zone A. The outliers in the

352   box plot reflect that the amount of K-feldspar porphyroclasts significantly decreases in

353   Zone B (Fig. 5B, C). In Zone C, it has the narrowest distribution in the three zones, and

354   there are hardly any K-feldspar porphyroclasts. The mean and median values of K-

355   feldspar grain size are 60 μm and 59 μm, respectively (Fig. 5B, C).
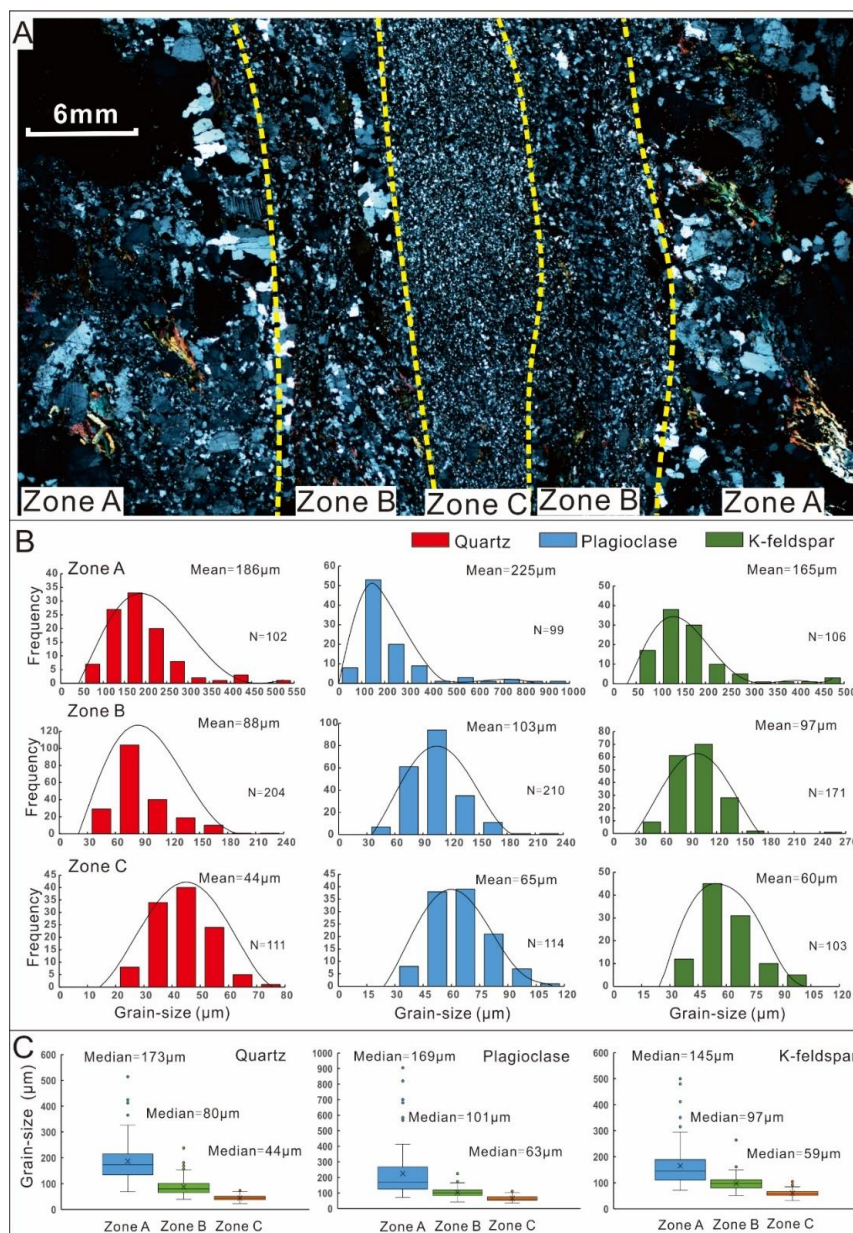
Fig.5. Mineral grain size evolution in the small-scale shear zone. (A) Thin-section scanning of small-scale shear zone. cross-polarized light micrographs. (B) Grain size distribution diagram of minerals in Zone A, B and C of small-scale shear zone. (C) The box-and-whisker diagram illustrates the results. Individual boxes were determined by their upper and lower quartiles, and the median was defined inside them. This progression of grain size is derived from CL pictures.

363

5. Mineral EBSD analysis in the small-scale shear zone

365   CPOs of quartz and feldspar were investigated mainly on the three zones (Zones A,
366 B, and C) of the micro-shear zone to further constrain the deformation conditions of the
367 small-scale shear zones. The results are illustrated in equal-area lower-hemisphere pole
368 figures.

5.1 Quartz and feldspar aggregates in the Zone A

370   In Zone A, the quartz grains mainly formed irregular polycrystalline aggregates,
371 and Dauphiné twins are occasionally observed in it (Fig. 6A). The pole figure of c-<0001>
372 axis exhibits a well-developed point maximum near the Y-axis, with a maximum value
373 of multiples of uniform distribution (MUD) of ~6.42. The pole figures of m-(10-10) and
374 a-(11-20) planes present a weaker girdle close to the XZ plane (Fig. 6B). In the sample
375 coordinate system (SCS), the low angle (2°-15° in this article) rotation axes demonstrate
376 high spatial density close to the Y-axis, consistent with the pole figure of the c-axis (Fig.
377 6C). The low angle rotation axes indicate high spatial density close to the c-axis in the
378 crystal coordinate system (CCS; Fig. 6C). In the misorientation angle distribution
379 histogram, the relative frequency of misorientation angles less than 15° is around 0.08,
380 and the relative frequency of misorientation angle of 60° is around 0.13 in the ~~corrected~~
381 pairs (Fig. 9A). The misorientation angle distribution of the ~~uncorrected~~ pairs exhibits
382 an irrelevance with the calculated random distribution curve (Fig. 9A).

383   The K-feldspar porphyroclasts gather into aggregates and are surrounded by large
384 quantities of small quartz and plagioclase grains in Zone A (Fig. 6A). The pole figure of
385 K-feldspar reveals a low maximum value of MUD, which is 2.69. The (100) plane forms
386 two maxima in the z-axis, while the pole figures of (010) and (001) planes form a point
387 maximum in the direction with a low angle to the x-axis (Fig. 6B). Although the rotation
388 axes present a point maximum between the X- and Z-axis in the SCS and a point
389 maximum close to the <001>-axis in the CCS, a clear clustering is not observed in the
390 low angle rotation axis distributions of K-feldspar (Fig. 6C). In the misorientation angle
391 distribution histogram, the distribution of misorientation angles of corrected pairs is
392 uniform except <15° and 180°, whose relative frequencies are much high than other
393 angles. The misorientation angle distribution of the ~~uncorrected~~ pairs reveals a positive
394 correlation with the calculated random distribution curve (Fig. 9B).

395   The shape of plagioclase grains is regular, and Albite twins are common in the
396 plagioclase grains in Zone A (Fig. 6A). The pole figure of plagioclase suggests a low
397 maximum value of MUD, which is 2.23. The plagioclase and K-feldspar have similar
398 crystallographic orientations in the (001) plane. The (010) plane forms a maximum

399   between the X- and Z-axis, and the (100) plane presents high spatial density near the Y
400   direction (Fig. 6B). In the SCS, the low angle rotation axes demonstrate high spatial
401   density in the position between the X- and Z-axis, and the low angle rotation axes reflect
402   high spatial density close to the <100>-axis in the CCS. The low angle rotation axis
403   distributions of plagioclase are also disorderly similar to K-feldspar's (Fig. 6C). In the
404   misorientation angle distribution histogram, the misorientation angle of 180° has the
405   highest relative frequency of around 0.15 in the ~~corrected~~ pairs. The misorientation angle
406   distribution of the ~~uncorrected~~ pairs exhibits a positive correlation with the calculated
407   random distribution curve. ~~The difference is that the random distribution curve~~
408   ~~rises linearly (Fig. 9C).~~
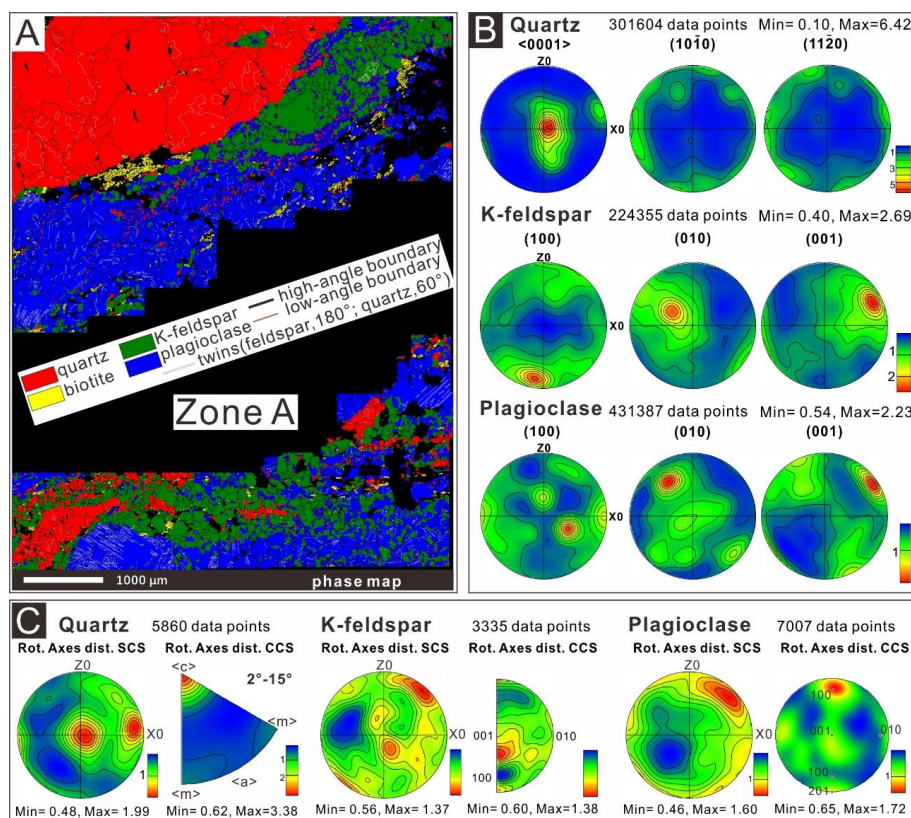
409

410   *Fig. 6. EBSD map and Quartz, K-feldspar and plagioclase crystallographic orientation*
411   *data in the Zone A. (A) EBSD phase map and grain boundary map. (B) Contoured pole*
412   *figures of quartz, K-feldspar, and plagioclase. (C) Rotation axes of 2°-15° distributions*
413   *for quartz, K-feldspar, and plagioclase in sample and crystal coordinate system. The*
414   *pole figures are plotted as one point per pixel. The pole figures and Rotation axes*
415   *distributions are projected to XZ plane at half width 25°, data clustering 5°. Red color*
416   *marks maxima, also given as multiples of the uniform distribution.*

5.2 Quartz ribbons and feldspar layers in the Zone B

In Zone B, the quartz irregular polycrystalline aggregates have disintegrated, and the content of quartz in the matrix is higher than those in Zone A (Fig. 7A). The pole figure of the c-axis reveals a well-developed point maximum in the Y-axis, with the maximum value of MUD of ~5.33. The pole figures of m- and a-plane show a weaker girdle in the XZ plane (Fig. 7B). In the SCS, the low angle rotation axes suggest high spatial density close to the Y-axis, similar to the pole figure of the c-axis (Fig. 6H). The low angle rotation axes exhibit high spatial density close to the c-axis in the CCS (Fig. 7C). In the misorientation angle distribution histogram, the relative frequency of the corrected pairs' misorientation angles (<15°) is also around 0.08, while the relative frequency of misorientation angles (60°) is around 0.12, which is less than the value in the Zone A. The misorientation angle distribution of the uncorrected pairs presents a negative correlation with the calculated random distribution curve (Fig. 9A).

In Zone B, the K-feldspar porphyroclasts are hardly observed, and the smaller grains gather into K-feldspar layers (Fig. 7A). The pole figure of K-feldspar reveals a low maximum value of MUD of ~2.14. The pole figure of the (100) plane forms a point maximum near the X-axis. The pole figures of (010) and (001) planes present weak patterns (Fig. 7B). The low angle rotation distributions indicate very scattered data, and the quantity of data points reduces to 70% compared to Zone A (Fig. 7C). The distribution of misorientation angles is also in line with those in Zone A, while the relative frequency of <15° and 180° is lower in the corrected pairs. The misorientation angle distribution of the uncorrected pairs exhibits a positive correlation with the calculated random distribution curve (Fig. 9B).

The pole figure of plagioclase reveals a low maximum value of MUD of ~1.90. The pole figure of the (001) plane forms maxima between the X- and Z-axis, and the pole figures of (100) and (010) planes present weak patterns (Fig. 7B). The low angle rotation distributions also indicate very scattered data, and the quantity of data points decreases to 40% compared with that of Zone A (Fig. 7C). The distribution of misorientation angles is consistent with those in Zone A, while the relative frequency of 180° is lower in the corrected pairs. The misorientation angle distribution of the uncorrected pairs demonstrates a positive correlation with the calculated random distribution curve. Besides, the random distribution curve rises linearly (Fig. 9C).
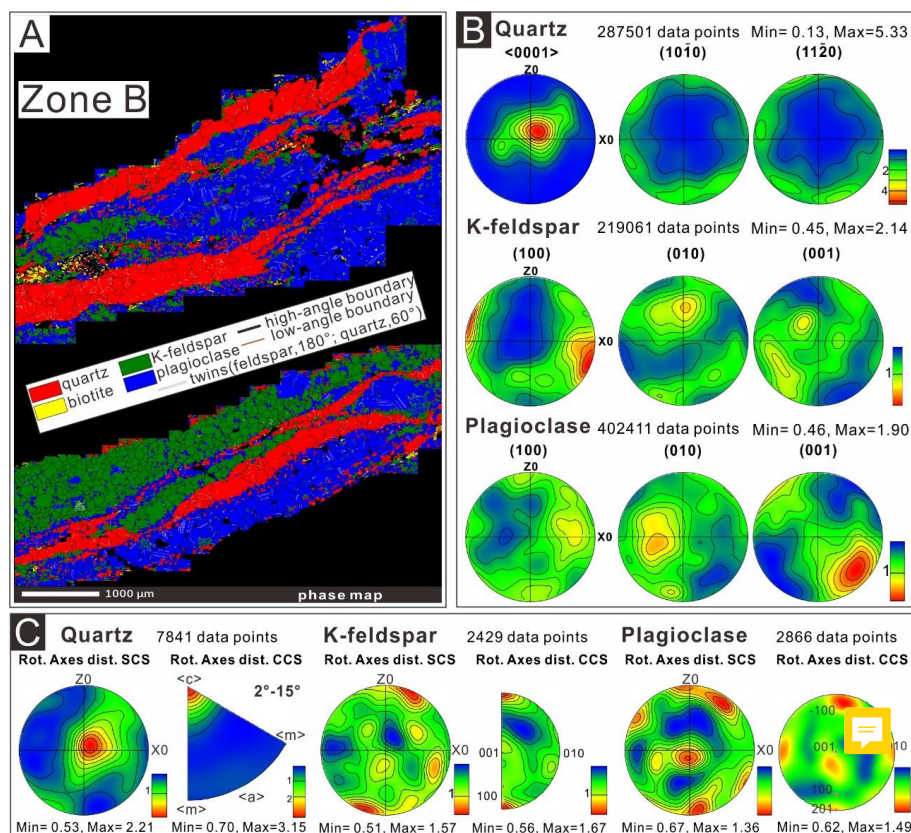
Fig. 7. EBSD map and Quartz, K-feldspar and plagioclase crystallographic orientation data in the Zone B. (A) EBSD phase map and grain boundary map. (B) Contoured pole figures of quartz, K-feldspar, and plagioclase. (C) Rotation axes of 2°-15° distributions for quartz, K-feldspar, and plagioclase in sample and crystal coordinate system. The pole figures are plotted as one point per pixel. The pole figures and Rotation axes distributions are projected to XZ plane at half width 25°, data clustering 5°. Red color marks maxima, also given as multiples of the uniform distribution.

5.3 Mixed matrix of quartz and feldspar in the Zone C

In Zone C, the quartz grains are completely disseminated among the other matrix phases (Fig. 8A). The pole figures suggest a low maximum value of MUD of ~1.50. A clear clustering is not observed in the pole figure of the c-axis. The pole figures of m- and a-plane present a weak and wide girdle in the XZ plane (Fig. 8B). The low angle rotation axes exhibit a maximum close to the c-axis in the CCS, while it is much weaker compared with Zones A and B (Fig. 8C). In the misorientation angle distribution histogram, the relative frequency of the ~~corrected~~ pairs' misorientation angles (<15°)

470 The feldspar grains are mixed with quartz grains in Zone C (Fig. 8A). The pole figure
471 of K-feldspar reveals a low maximum value of MUD of ~1.67 (Fig. 8B). The low angle
472 rotation distributions also suggest very scattered data without a clear clustering (Fig. 8C).
473 In the misorientation angle distribution histogram of corrected pairs, the relative
474 frequency of misorientation angles (180°) is low. The misorientation angle distribution
475 of the uncorrected pairs exhibits a positive correlation with the calculated random
476 distribution curve (Fig. 9B). The pole figure of plagioclase demonstrates a low maximum
477 value of MUD of ~2.37. The feature of the pole figure of the (001) plane is consistent
478 with that in Zone B (Fig. 8B). However, the low angle rotation distributions reflect few
479 scattered data (Fig. 8C). The relative frequency of misorientation angles (180°) is around
480 0.10 in the misorientation angle distribution of corrected pairs. The uncorrected pairs
481 present a positive correlation with the calculated random distribution curve. Additionally,
482 the random distribution curve also rises linearly (Fig. 9C).
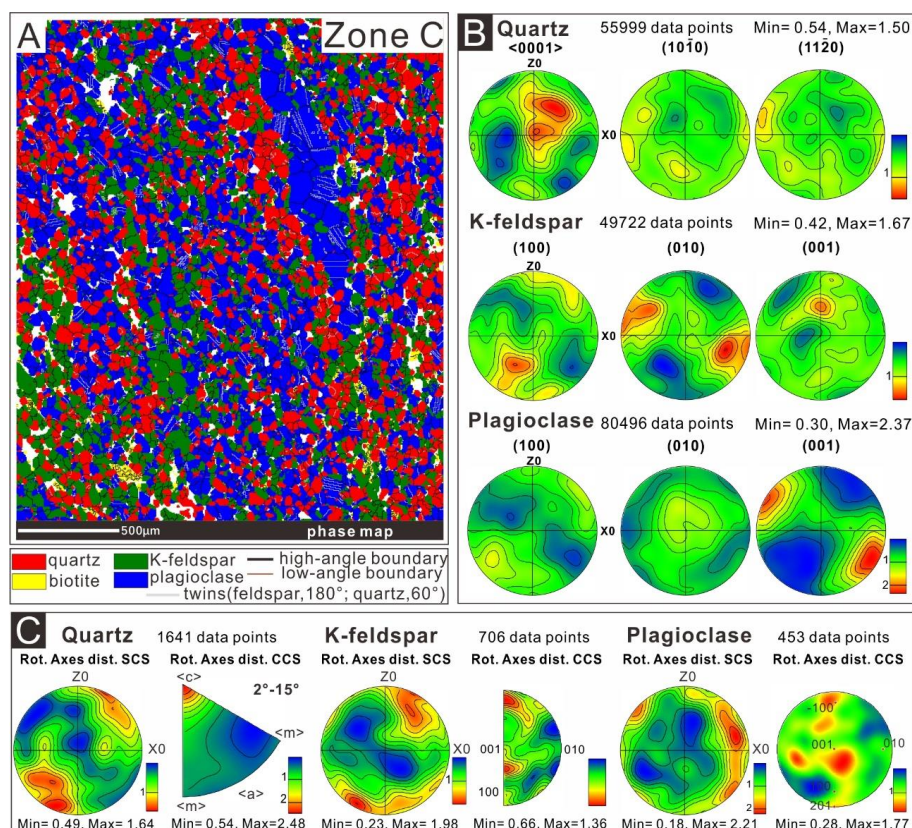
484 *Fig. 8. EBSD map and Quartz, K-feldspar and plagioclase crystallographic orientation*

485 *data in the Zone B. (A) EBSD phase map and grain boundary map. (B) Contoured pole*

486 *figures of quartz, K-feldspar, and plagioclase. (C) Rotation axes of 2°-15° distributions*

487 *for quartz, K-feldspar, and plagioclase in sample and crystal coordinate system. The*

488 *pole figures are plotted as one point per pixel. The pole figures and Rotation axes*

489 *distributions are projected to XZ plane at half width 25°, data clustering 5°. Red color*

490 *marks maxima, also given as multiples of the uniform distribution.*
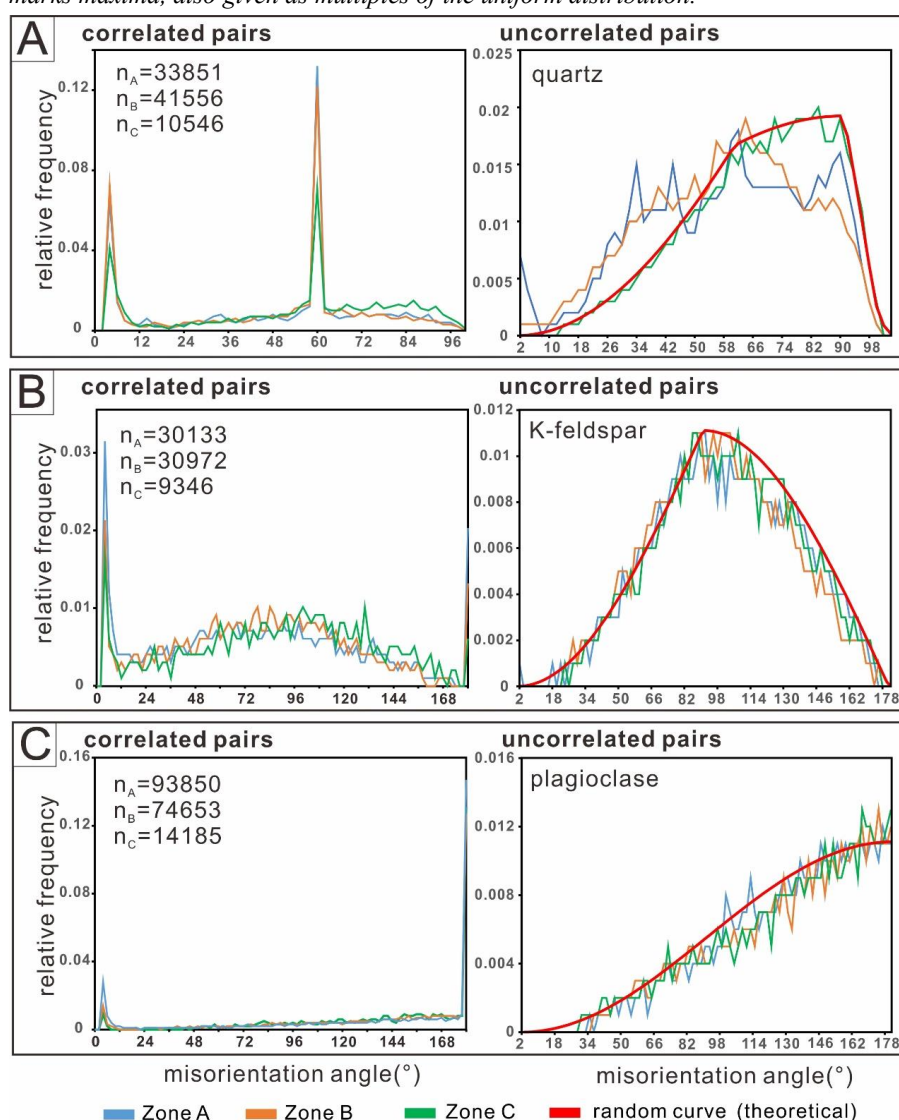
492 *Fig. 9. Misorientation angle distribution for correlated and uncorrelated pairs of Fig.6.*

493 *(A) quartz, (B) K-feldspar, and (C) plagioclase in the Zone A, Zone B and Zone C. Solid*

494 *blue lines mark the mineral misorientation angle distribution in Zone A; Solid orange*

495 *lines mark the mineral misorientation angle distribution in Zone B; Solid green lines*

496 *mark the mineral misorientation angle distribution in Zone C. Solid red line marks the*
497 *calculated random distribution and the number of statistics is 10000 in the random*
498 *misorientation. In the correlated misorientation, n_A= the number of statistics in Zone A,*
499 *n_B= the number of statistics in Zone B, n_C= the number of statistics in Zone C.*
500

501 ### 6. Thermobarometry of the granodiorite

502 **6.1 P-T estimation**
503 Hornblende-plagioclase thermometry is frequently utilized in granites and gneisses
504 with coexisting hornblende and plagioclase to estimate temperature and pressure in
505 magma crystallization or subsequent metamorphism (Schmidt, 1992; Popp et al., 1995;
506 Ridolfi and Renzulli, 2011; Dong et al., 2021). Mineral chemistry was determined on
507 unfoliated granodiorite at the GLG-SZ boundary and on foliated granitic rocks within
508 the GLG-SZ. Experiments were conducted on hornblende grains combined with quartz
509 or plagioclase under the premises for Al-in-hornblende barometry application (Hollister
510 et al., 1987; Schmidt, 1992; Popp et al., 1995; Stein and Dietl, 2001; Ridolfi and Renzulli,
511 2011). In this study, the hornblende-plagioclase geothermometer designed by Holland
512 and Blundy (1994) is employed to determine the temperature. These calculations were
513 based on hornblende solid-solution models and well-constrained natural systems. The
514 temperatures and pressures of the unfoliated granitoids are T = 641–730 °C with an
515 average of T = 673 °C, P = 4.0–5.9 kbar with an average of P =5.1 kbar (Fig. 10A). The
516 crystallization P-T values for the foliated granitic rocks are T = 658–736 °C with an
517 average of T = 710 °C, P = 2.1–2.9 kbar with an average of P = 2.7 kbar (Fig. 10B)

518 **6.2 Emplacement depth**
519 The crystallization pressures for the investigated granodiorite are calculated by the
520 method developed by Anderson and Smith (1995). It is possible to estimate the pressure
521 with an error of about 0.6 kbar using the method proposed by Popp et al. (1995). This
522 error corresponds to about 2.10 km in depth. The density assumption of 2.8 g/cm^3 is used
523 for the GLG-SZ in our calculations to convert the pressures measured to emplacement
524 depths. After the temperature adjustment, the calculated unfoliated granitoids' pressures
525 range from 4.0 ± 0.6 kbar to 5.8 ± 0.6 kbar, implying that emplacement depths range
526 from 14.3 ± 2.1 km to 20.7 ± 2.1 km, and the average depth is 17.5 km (Fig. 10A). The
527 calculated pressures in the foliated granitic samples change from 2.2 ± 0.6 kbar to 2.9 ±
528 0.6 kbar, suggesting that emplacement depths vary from 7.8 ± 2.1 km to 10.3 ± 2.1 km,
529 and the average depth is 9.0 km (Fig. 10B).
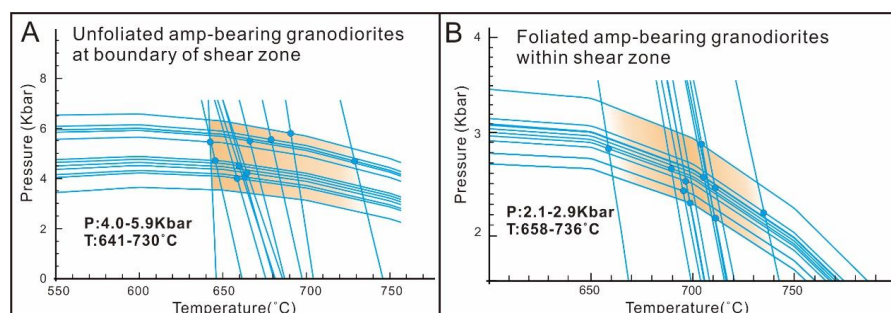
531 *Fig. 10. Pressure-temperature diagram of unfoliated granitoids at boundary of GLG-SZ*
532 *and foliated granitic rocks within GLG-SZ.*

533

534 **7. Paleopiezometry**

535 **7.1 Flow stress estimate from recrystallized quartz grains**

536   The grain size of dynamically recrystallized quartz varies with differential stress in
537 plastic deformation and is used as a method for calibrating the magnitude of paleostress
538 (Mercier et al., 1977; Twiss, 1977; Twiss, 1980; Koch, 1983; Boutonnet et al., 2013).
539 This study only considered dynamically recrystallized quartz grain sizes from the small-
540 scale shear zones for estimating paleostress. The optical size of recrystallized grains was
541 determined with standard petrographic microscopy. Measurements were performed with
542 each grain perpendicular to macroscopic foliation and parallel to macroscopic lineation
543 (Behrmann and Seckel, 2007). The results of the analysis are listed in Table 1. The
544 standard error of the differential stress estimates is less than 15%.

545   The differential stress is estimated through piezometer calibration (Stipp and Tullis,
546 2003), followed by a calibration corrected by Holyoke and Kronenberg (2010). The low-
547 strain domain (Zone A) average size is 165 μm; the differential flow stress is 12 MPa
548 (Stipp and Tullis, 2003) and 9 MPa (Holyoke and Kronenberg, 2010). The medium-strain
549 domain (Zone B) average size is 78 μm; the differential flow stress is 21 MPa (Stipp and
550 Tullis, 2003) and 15 MPa (Holyoke and Kronenberg, 2010). The high-strain domain
551 (Zone C) average size is 44 μm; the differential flow stress is 33 MPa (Stipp and Tullis,
552 2003) and 24 MPa (Holyoke and Kronenberg, 2010). However, uncertainties remain in
553 the estimation of flow stress from the mineral grain sizes that can be affected by the
554 presence of other phases and notably fluid during deformation.

555 **7.2 Flow stress estimate from recrystallized grain size**
556   Estimating the strain rate is a critical step in comprehending deformation processes.
557 The relationships between temperature, microstructures, and CPO patterns
558 corresponding to the dominant slip systems indicate deformation under amphibolite-

559 facies conditions at temperatures of ca. 400 °C–700 °C in the small-scale shear zones
560 (Hirth and Tullis, 1992; Stipp et al., 2002). In this study, strain rates of quartz grains at
561 temperatures of ca. 550°C were constructed. Ductile creep curves were calculated for
562 strain rates from 10^{-10} to 10^{-16} S^{-1} following the flow law from Luan and Peterson (1992)
563 and the wet quartzite flow law of Hirth et al. (2001). In the calculation, the effect of water
564 fugacity was considered, though the dependence of strain rate on water fugacity was not
565 determined in the original paper. When it was applied to the differential stress estimates
566 from dynamically recrystallized grain sizes of quartz by the piezometer (Stipp and Tullis,
567 2003; Holyoke and Kronenberg, 2010), strain rates estimated in Zone A are 4.75×10^{-16}
568 S^{-1} to 1.17×10^{-14} S^{-1}, strain rates estimated in Zone B are 5.13×10^{-15} S^{-1} to 1.26×10^{-13}
569 S^{-1}, and strain rates estimated in Zone C are 3.16×10^{-14} S^{-1} to 7.75×10^{-13} S^{-1}. The
570 average strain rate estimated in Zone A is 4.29×10^{-15} S^{-1}, the average strain rate
571 estimated in Zone B is 4.62×10^{-14} S^{-1}, and the average strain rate estimated in Zone C
572 is 2.85×10^{-13} S^{-1}.

573 **Table 1**

574 Paleopiezometry data for quartz and deduced strain rates in the small-scale shear zone.

575

Domain	Recrystall. regime	Apparent grainsize (microns)	Paleopiez- ometer	Stress (MPa)	T (°C)	Flow law	Strain rate (1/s)
Zone A	GBM	165	ST-2003	12	550	H-2001 LP-1992	1.17E-14 1.67E-15
			SH-2010	9	550	H-2001 LP-1992	3.33E-15 4.75E-16
Zone B	GBM+GBS	78	ST-2003	21	550	H-2001 LP-1992	1.26E-13 1.80E-14
			SH-2010	15	550	H-2001 LP-1992	3.59E-14 5.13E-15
Zone C	GBM+GBS	44	ST-2003	33	550	H-2001 LP-1992	7.75E-13 1.11E-13
			SH-2010	24	550	H-2001 LP-1992	2.21E-13 3.16E-14

576 *Stress estimated using differential piezometer, ST-2003-Stipp and Tullis, 2003*
577 *and SH-2010-Koch, 1983. H-2001 flow law is referenced to Hirth et al., 2001, LP-*
578 *1992 flow law is referenced to Luan and Peterson, 1992.*

579

8. Discussions

8.1 Significance of quartz CPOs within the small-scale shear zone

582 Before this study, the detailed characteristics and conditions of deformation and
583 CPOs of minerals (quartz and feldspar) in the small-scale shear zone were largely

584 undocumented and discussed, though numerous data on structures, microfabrics, and
585 geochronology have been published from the GLG-SZ show Cenozoic high-temperature
586 ductile deformation conditions (Zhang et al., 2012b; Xu et al., 2015; Dong et al., 2019).
587 The small-scale shear zone developing in the unfoliated granodiorite presents a
588 significant decrease in grain size from the rim (Zone A) to center (Zone C) with
589 increasing strain. In the low-strain domains of Zones A and B, the quartz polycrystalline
590 aggregated ribbons are characterized by grain boundary migration recrystallization
591 (GMR), revealing a medium-high temperature plastic-deformation condition (Fig.3,6
592 and 7; Hippertt et al., 2001; Stipp et al., 2002; Passchier and Trouw, 2005; Holyoke and
593 Tullis, 2006; Hansen et al., 2013; Cavalcante et al., 2018; Dong et al., 2019).

594   The deformation conditions can be recorded by developed dominated slip systems
595 of deformed quartz grains, which are normally temperature-sensitive (Stipp et al., 2002).
596 Prism <a> slip occurs frequently in high-grade metamorphic rocks (Cao et al., 2011b,
597 2013a, b), while basal <a> slip appears in low-grade or overprinted metamorphic rocks
598 (Toy et al., 2008; Cao et al., 2010, 2011b; Cheng et al., 2018). The low angle rotation
599 axis distribution and the C-axis patterns of quartz grains from the three zones in the
600 small-scale shear zone display dominated the high-temperature prism <a>slip system
601 (Fig. 6, 7). However, the quartz c-axis patterns in Zones A and B are more intensive, with
602 the Max between 5.33 and 6.42. The misorientation angle distribution of uncorrelated
603 grain pairs does not conform to the random curve (Fig. 7A).

604   All these results suggest that the quartz grains in the small-scale shear zone have
605 undergone significant high temperature (>400–700°C) dislocation creep deformation,
606 similar to the GLG-SZ (Dong et al., 2019). However, the quartz c-axes pattern in Zone
607 C demonstrates the weaker intensive of 1.50 (Fig. 8B). The effects of intragranular
608 deformation are dramatically reduced (Fig. 9A). Certain minerals from the high-strain
609 zone C are completely transformed into ultramylonites generated by extremely fine
610 grains. Ultra-plastic flow is an essential process of quartz deformation in the high-strain
611 domain within the shear zone.

8.2 Mechanism of feldspar deformation and changed CPO patterns

613   Studies have demonstrated that feldspars have different deformation behaviors
614 and mechanisms, including brittle fracturing and cataclastic flow in the shallow crustal
615 low-temperature conditions and dynamic recrystallization associated grain-size
616 reduction under the high-temperature conditions (Olsen and Kohlstedt, 1984; Olsen and
617 Kohlstedt, 1985; Tullis and Yund, 1987, 1991; Wintscha and Yi, 2002; Mancktelow and
618 Pennacchioni, 2004; Dang et al., 2017; Menegon et al., 2017; Mansard et al., 2018; Dong
619 et al., 2019). In the studied small-scale shear zone, the feldspar grains present the well-
620 marked variation of compositions and grain sizes from the undeformed magmatic texture
621 to typical crystal plastic flow deformation, revealed by the microstructure, CL, and CPO

properties (Fig. 3). In the low-strain domain of Zone A, undulatory and inhomogeneous extinction are common in the porphyroclastic feldspar grains. Occasionally, the feldspar grains exhibit irregular and sharpened grain boundaries. Most K-feldspar porphyroclasts display elongation and grain-size reduction by dynamic recrystallization. The dynamic recrystallization grains occur in the asymmetric porphyroclast (e.g., hornblende and feldspar) tails with neocrystallization aggerates, which extend to the shear zone's mylonitic foliation/lineation. The K-feldspar porphyroclasts are surrounded by quartz, plagioclase, or K-feldspar fine grains, establishing a typical core-mantle structure (Fig. 4A, B). With an increase in the strain, the feldspar porphyroclasts disintegrate, and the fine feldspar grains gather to layered aggregates with an orientation nearly parallel to the mylonitic foliation (Fig. 4E). Fractures or mechanical twins can be observed in a small amount of large K-feldspar porphyroclasts (Fig. 3D).

Under medium-high temperature deformed conditions, the deformation mechanism of K-feldspar is mainly attributed to activation slip systems of (010) <101> or <100> (Tullis,1983; Gandais and Willaime, 1984; Franěk et al., 2006; Ishii et al., 2007; Menegon et al., 2008). Besides, (100) <010> slip occurs in K-feldspar zones under upper greenschist facies condition (Ishii et al., 2007). However, plagioclase often reflects main slip systems of (010) <001> and (001) <110>, while (001) <100>, (010) <100>, and (111) <110> slips develop slip at higher metamorphic conditions (Svava et al., 1985; Kruhl et al., 1987; Ji et al., 1988; Mainprice et al., 1989; Heidelbach et al., 2000; Kruse et al., 2001; Egydio-Silva et al., 2002; Stünitz et al., 2003; Passchier and Trouw, 2005). Under higher-grade metamorphic conditions or intense grain-size reduction and phrase mixing, diffusion creep is a more critical deformation mechanism (Gower and Simpson, 1992; Menegon et al., 2008, 2013; Czaplińska et al., 2015; Miranda et al., 2016; Dong et al., 2019). In the low-strain domain (Zone A), the EBSD analysis suggests that the dominant slip system in K-feldspar is (100) <010>, and the dominant slip system in plagioclase is (010) <001> (Fig.6B, C). The high proportion of low-angle misorientation angles of plagioclase and K-feldspar demonstrates the development of intragranular deformation (Fig.9B, C). Thus, the dislocation creep is the dominant mechanism in feldspar deformation within the low-strain domain (Altenberger and Wilhelm, 2000; Menegon et al., 2017). However, the random distribution of feldspar grains cannot be explained by dislocation creep and the formation of myrmekites induced by dynamic recrystallization. These features imply another mechanism during the feldspar deformation in the low-strain domain. They are formed by dissolution-precipitation creep (Menegon et al., 2008; Dong et al., 2019) for the result of grain-boundary diffusion (Ishii et al., 2007).

In the high-strain domain (Zone C), intense grain-size reduction of minerals generated ultramylonites with the increasing strain. Ultra-plastic flow is a crucial process of deformation in the high-strain domain within the shear zone. The fine-grained feldspar

660 displays (1) a weak CPO (Fig. 8B); (2) equant to slightly elongated shape (Fig. 5, 8A);
661 (3) rare low-angle grain boundaries (Fig. 8C, 9); (4) uncorrelated misorientation angle
662 distributions close to the theoretical random-pair distribution (Fig. 9). This alignment of
663 grains parallel to the displacement direction is frequently reported in materials deforming
664 with a contribution of grain boundary sliding (GBS; e.g., Drury and Humphreys, 1988;
665 Stünitz and J.D., 1993; Fliervoet et al., 1997; Kilian et al., 2011; Mansard et al., 2018).
666 The weakening of CPOs, phase mixing, and grain size reduction suggest that grain
667 boundary sliding (GBS) becomes increasingly active and an essential deformation
668 mechanism (Passchier and Trouw, 2005; Langdon, 2006; Fusseis et al., 2009; Kilian et
669 al., 2011; Platt, 2015; Miranda et al., 2016; Mansard et al., 2018).

8.3   Deformation associated fluid of the small-scale shear zone

671 Recognizing the evolution of small-scale ductile shear zone is also particularly
672 valuable for the understanding of the processes of shear localization in the middle and
673 lower crusts (Mancktelow and Pennacchioni, 2005, 2013; Pennacchioni, 2005; Kilian
674 et al., 2011; Pennacchioni and Mancktelow, 2018), as well as interpreting shear zone
675 history regarding P-T-fluid evolution along strain gradients (Bestmann and
676 Pennacchioni, 2015; Cao and Neubauer, 2016). Hydrolytic weakening has been
677 demonstrated to be a major process facilitating strain localization (Finch et al., 2016;
678 Cao et al., 2017). Fluid can weaken rocks or minerals in several methods (Sibson, 1977;
679 Mancktelow and Pennacchioni, 2004; Kohlstedt, 2006; Kilian et al., 2011; Oliot et al.,
680 2014; Finch et al., 2016; Cao et al., 2017; Cheng et al., 2018). This is in that the fluid in
681 crystals can weaken the mechanical strength of crystals by decreasing the strength of
682 Si-O bonds. It allows easier glide of dislocations (Kohlstedt, 2006) and diffusion at
683 lower temperatures (Sibson, 1977). Intergranular fluid results in nucleation of new
684 grains in cavities by mass transfer, contributing to accelerating grain boundary sliding
685 (GBS) and reducing the intercrystalline rock strength (Chen and Argon, 1979;
686 Kronenberg, 1994; Mancktelow and Pennacchioni, 2004; Kilian et al., 2011). The
687 relevant evidence from low-strain (Zone A) or medium-strain domains (Zone B) reveals
688 that quartz and mica grains of extremely small size (ca. 20μm) occur at the fine-grained
689 plagioclase aggregates or at the junctions of K-feldspar grains (Fig. 11). This kind of
690 feature can be explained by fluid-accommodated grain boundary sliding (GBS). The
691 incomplete displacement along grain boundaries by GBS can trigger the opening of the
692 cavities and leads to the ingress and diffusion of the material (Fliervoet et al., 1997;
693 Passchier and Trouw, 2005; Kilian et al., 2011; Platt, 2015; Finch et al., 2016; Menegon
694 et al., 2017; Precigout et al., 2017; Mansard et al., 2018). The neocrystallization grains
695 pin in cavities restrains grain growth by impeding grain boundary migration and
696 arresting the original grain size at the approximate size of the dynamic recrystallization
697 new grains. The grain size reduction and the increase of phase mixing can further

698   weaken rock and strain localization in the small-scale shear zones.

699   Intergranular fluid also reduces the intercrystalline rock strength by metamorphic

700   reaction (White and Knipe, 1978; Hippertt, 1998; Oliot et al., 2014; Spruzeniece and

701   Piazolo, 2015; Liu, 2017). For example, the retrogressive metamorphism of hornblende

702   and involved water can produce the weaker phase as biotite and quartz (Fig.4C; Liu,

703   2017). The studied small-scale shear zones reveal the distinct evidence of strain

704   localization accompanied by hydrous retrogression of hornblende to interconnected

705   weaker mica parallel to the main ultramylonitic foliation. That mica presents the visible

706   appearance from undeformed magmatic phases to ductile deformed phases. The biotite

707   occurs as undeformed or slightly bent magmatic phases in the studied unfoliated

708   granodiorite (Fig. 3), generally regarded as the weakest phase (Tullis and Wenk, 1994).

709   As the strain increases, the micas in the low-strain domain break into small pieces, and

710   several mica pieces are parallel to each other which cut across quartz-rich layers. With

711   further localization, a network of monophase biotite layers starts to form in the medium-

712   strain domain of Zone B (Fig. 3G). The interconnected mica layers can be frequently

713   formed during crystal plastic deformation. Additionally, a portion of biotite appears at

714   the quartz and plagioclase grain boundaries (Fig. 4). In the high-strain domain, the

715   network of micas is destroyed, and the mica grains are disseminated in the matrix (Fig.

716   4C, 11C). This presents similar distributed features to diffusion creep (Fliervoet et al.,

717   1997; Herwegh and Jenni, 2001). The microstructure characteristics imply that the

718   formation of biotite can soften the rock's matrix, resulting in increased deformation

719   intensity (Mancktelow, 2008; Fossen and Cavalcante, 2017; Mansard et al., 2018).

720
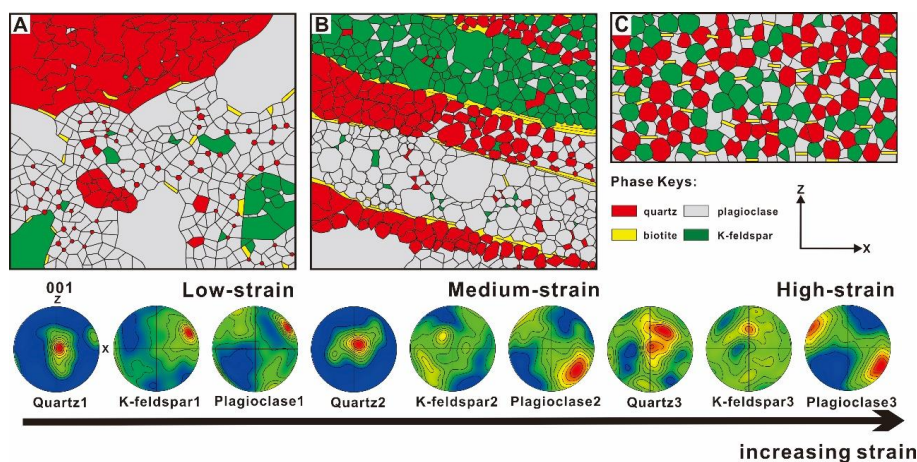
721   *Fig. 11. Representative maps of the different strain domain that have been manually*

722   *digitized and the variety of mineral c-axis orientation in the small-scale shear zone (A)*

723   *Low-strain domain which is closed with wall-rock. (B) Medium-strain domain which is*

724   *strip in shape. (C) High-strain domain which is mixed-phase zone.*

8.4 Formation conditions and processes of the small-scale shear zone

Microstructural analyses of the small-scale shear zones reveal ductile deformation processes in the deep-seated crust. The unfoliated granitoids have an average emplacement depth of 18 km. Macro- and micro-structures apparently reveal progressive plastic deformation behaviors of the major mineral phases (quartz, feldspar, hornblende, and mica) in response to a progressive ductile deformation history of the small-scale shear zone (Fig. 11). The results demonstrate that the small-scale shear zone has experienced high-temperature deformation conditions at least amphibolite facies during the dominant ductile shearing. The small-scale shear zones and the foliated granodiorite within the GLG-SZ exhibit identical synkinematic metamorphic assemblages and microstructures (Fig.3; Dong et al., 2019, 2021). In other words, they formed under similar metamorphic and deformation conditions. The temperature conditions of foliated granodiorite are determined based on hornblende-plagioclase thermometry to be 670–735 °C (Fig. 10B). Similar temperature conditions are inferred in the small-scale shear zones. The development of myrmekite and the recrystallization of quartz also can verify the high-temperature metamorphic conditions in the small-scale shear zones (Figa.3&4; Wirth and Voll, 1987; Tribe and D'Lemos, 1996; Ceccato et al., 2018). The initiation of prism <a> slip and the features of grain boundary migration recrystallization of quartz grains confirm that the small-scale shear zones formed at the medium-high temperature condition (Fig.6; Hobbs, 1985; Mainprice et al., 1986; Stipp and Tullis, 2003; Passchier and Trouw, 2005; Toy et al., 2008; Gibert and Mainprice, 2009; Xia and Liu, 2011).

Generally, rheological weakening mechanisms play a significant role in the localization of shear zones, as shear zones typically form in the weakest zone (Schmid et al., 1996; Imber et al., 1997; Rosenberg, 2004; Dayem et al., 2009; Yamasaki et al., 2014; Cao and Neubauer, 2016; Fossen and Cavalcante, 2017; Liu, 2017; Pennacchioni and Mancktelow, 2018). Besides temperature and pressure, several other factors such as mineralogy, strain rate, microstructure, texture, and fluid that can weaken mechanisms are activated during strain localization (Mancktelow and Pennacchioni, 2004; Oliot et al., 2014; Cao and Neubauer, 2016; Finch et al., 2016; Fossen and Cavalcante, 2017; Liu, 2017; Pennacchioni and Mancktelow, 2018). Localization may be caused by an external inhomogeneity such as a precursor fracture or joint, according to the macroscopic shear zone distribution and orientation similar to joint orientations in the same rock (Menegon and Pennacchioni, 2009). In this study, microstructural observations imply that the switch of deformation characteristics from wall rocks to the high-strain domain cannot be explained by the "precursor effect" (Fig. 3D). This inference cannot be confirmed by the varying orientation of small-scale shear zones (Fig. 1C). The high-temperature deformation conditions suggest that the initiation of the small-scale shear zones is at

763 depth, where temperature-controlled rheological weakening mechanisms play an
764 essential role in localizing future shear zones. Thermal heterogeneities of the lithosphere
765 can lead to shear concentration along hot-to-cold contacts ascribed to thermally enhanced
766 rheological weakening. Hence, rheological weakening by heterogeneities may induce
767 strain localization and increase strain rates within magmatic rocks bearing shear zones
768 t(Cao and Neubauer, 2016; Fossen and Cavalcante, 2017; Liu, 2017). The fast strain rate
769 within the high-strain domain of the small-scale shear zone is the consistent geological
770 evidence (Table 1). Thus, the deformation in the small-scale shear zones would be
771 localized to a narrow site through thermal-enhanced rheological weakening mechanisms
772 when GLG-SZ is deformed.

773 Interestingly, the strain rates gradually decrease from the high-strain (2.85×10^{-13}
774 S^{-1}) to the low-strain domain ($4.29 \times 10^{-15} S^{-1}$) in the small-scale shear zone. It can be
775 explained by the model of shear zone widening during shear deformation (Oliot et al.,
776 2014) after the influence of temperature is eliminated. The center of a shear zone
777 generally presents extreme grain-size reduction, involving fluid-assisted granular flow
778 deformation. The GBS can facilitate fluid migration through shear zones by causing
779 cavities to open and closure, which in turn induces fluids to be pumped through the rock
780 (Fliervoet et al., 1997; Passchier and Trouw, 2005; Kilian et al., 2011; Finch et al., 2016;
781 Menegon et al., 2017; Mansard et al., 2018). This created a pressure gradient, which
782 expelled fluids, leading to hydraulic microfracturing, metasomatism, host rock
783 weakening, and shear zone widening (Oliot et al., 2010, 2014; Finch et al., 2016). In the
784 small-scale shear zone, the localized deformation provoked the release of intracrystalline
785 water to grain boundaries and the migration of water to less deformed rocks, widening
786 the shear zones. Fluid content could restrict weak rheology in the widened shear zone
787 and decrease strain rates. This is also the reason for the grain size stratification of small-
788 scale shear zones (Fig. 11). Field observations and microstructural observations reveal
789 that the kinematic directions of the small-scale shear zone and the continental-scale
790 GLG-SZ are consistent (Fig. 3), reflecting that small-scale shear zones are controlled by
791 the GLG-SZ during progressive deformation and exhumation. The geothermal data
792 demonstrate that the foliated granitic rocks have occurred at least 9 km of vertical
793 displacement in GLG-SZ. The intrusion depth to the shearing depth may be related to
794 the GLG-SZ tectonic shearing and exhumation (Fig. 10). It also produces a lower
795 temperature condition in granitoids where brittle deformation can occur. Thus, the small-
796 scale shear zone activates as a fault and makes the mafic enclaves cut in the outcrop-
797 scale (Fig.2G).

10. Conclusions

799 The analyses of meso- and micro-structural, EBSD texture, paleopiezometry, and
800 thermobarometry lead to the following conclusions:

(1)   The small-scale shear zones at the boundary of GLG-SZ have experienced vibrations deformation, mineral composition, and fabric transition from the rim zone of protomylonite to the center zone of ultramylonites, accompanied by a significant grain-size reduction and progressive phase mixing of minerals with an increase in the strain.

(2)   The progressive development of microstructures suggests that the ductile deformation of small-scale shear zone is at least amphibolite facies conditions. Rheological weakening due to thermal heterogeneities induces strain localization, resulting in the initiation of the small-scale shear zone.

(3)   The deformation mechanism of the coarse-grained aggregate zone in the shear zone is dominated by dislocation creep, while the polyphase fine-grained mixed zone possesses the dominant mechanism of viscous grain boundary sliding. Fluid-assisted deformation plays a crucial role in the hydrous retrogression and subsequent flow rheological weakening of the shear-zone.

(4)   The deformation of the small-scale shear zone within the unfoliated granodiorite is controlled by the continental GLG-SZ. The small-scale shear zones experience the same kinematic direction of ductile shearing at depth and during exhumation, as well as the GLG-SZ.

Author contributions: Shuyun Cao and Lefan Zhan planned the overarching research goals and aims; Yanlong Dong, Wenyuan Li and Lefan Zhan performed the measurements and took the samples; Lefan Zhan analyzed the data; Lefan Zhan wrote the manuscript draft; Shuyun Cao, Yanlong Dong, Wenyuan Li and Lefan Zhan reviewed and edited the manuscript.

Acknowledgments: We gratefully acknowledge Prof. Pennacchioni G. for a lot of discussions and together for field trip. This work was financially supported by National Natural Science Foundations of China (Grant no. 41972220; 4188810) and National Key Research and Development Program (Grant no. 2017YFC0602401) and the Excellent Youth Fund of National Natural Science Foundation of China (Grant no. 41722207).

REFERENCES

Abers, G.A., van Keken, P.E., Wilson, C.R.: Deep decoupling in subduction zones: Observations and temperature limits, Geosphere, 16, 1408-1424, 2020.

Altenberger, U., Wilhelm, S.: Ductile deformation of K-feldspar in dry eclogite facies shear zones in the Bergen Arcs, Norway, Tectonophysics, 320, 107-121, 2000.

Behrmann, J.H., Seckel, C.: Structures, flow stresses, and estimated strain rates in metamorphic rocks of the Small Cyclades Islands Iraklia and Schinoussa (Aegean Sea, Greece), Geotectonic Research, 95, 1-11, 2007.

839   Bense, V.F., Gleeson, T., Loveless, S.E., Bour, O., Scibek, J.: Fault zone hydrogeology,
840   Earth-Sci. Rev., 127, 171-192, 2013.

841   Bestmann, M., Pennacchioni, G.: Ti distribution in quartz across a heterogeneous shear
842   zone within a granodiorite: The effect of deformation mechanism and strain on Ti
843   resetting, Lithos, 227, 37-56, 2015.

844   Bhattacharya, A.R., Weber, K.: Fabric development during shear deformation in the
845   Main Central Thrust Zone, NW-Himalaya, India, Tectonophysics, 387, 23-46, 2004.

846   Bistacchi, A., Massironi, M., Menegon, L.: Three-dimensional characterization of a
847   crustal-scale fault zone: The Pusteria and Sprechenstein fault system (Eastern Alps),
848   J. Struct. Geol., 32, 2022-2041, 2010.

849   Blundy, J.D., Holland, T.J.B.: Calcic amphibole equilibria and a new amphibole-
850   plagioclase geothermometer, Contrib. Mineral. Petrol., 104, 208-224, 1990.

851   Bons, P.D., Jessell, M.W.: Micro-shear zones in experimentally deformed
852   octachloropropane, J. Struct. Geol., 21, 323-334, 1999.

853   Brown, M., Solar, G.S.: Shear-zone systems and melts: feedback relations and self-
854   organization in erogenic belts, J. Struct. Geol., 20, 211-227, 1998.

855   Cao, S., Liu, J., Leiss, B.: Orientation-related deformation mechanisms of naturally
856   deformed amphibole in amphibolite mylonites from the Diancang Shan, SW Yunnan,
857   China, J. Struct. Geol., 32, 606-622, 2010.

858   Cao, S., Liu, J., Leiss, B., Neubauer, F., Genser, J., Zhao, C.: Oligo-Miocene shearing
859   along the Ailao Shan–Red River shear zone: Constraints from structural analysis and
860   zircon U/Pb geochronology of magmatic rocks in the Diancang Shan massif, SE
861   Tibet, China, Gondwana Res., 19, 975-993, 2011.

862   Cao, S., Neubauer, F.: Deep crustal expressions of exhumed strike-slip fault systems:
863   Shear zone initiation on rheological boundaries, Earth-Sci. Rev., 162, 155-176, 2016.

864   Cao, S., Neubauer, F., Bernroider, M., Liu, J.: The lateral boundary of a metamorphic
865   core complex: The Moutsounas shear zone on Naxos, Cyclades, Greece, J. Struct.
866   Geol., 54, 103-128, 2013a.

867   Cao, S., Neubauer, F., Bernroider, M., Liu, J., Genser, J.: Structures, microfabrics and
868   textures of the Cordilleran-type Rechnitz metamorphic core complex, Eastern Alps,
869   Tectonophysics, 608, 1201-1225, 2013b.

870   Cao, S., Neubauer, F., Liu, J., Bernroider, M., Cheng, X., Li, J., Yu, Z., Genser, J.:
871   Rheological weakening of high-grade mylonites during low-temperature
872   retrogression: The exhumed continental Ailao Shan-Red River fault zone, SE Asia,
873   J. Asian Earth Sci., 139, 40-60, 2017.

874   Cavalcante, C., Lagoeiro, L., Fossen, H., Egydio-Silva, M., Morales, L.F.G., Ferreira, F.,
875   Conte, T.: Temperature constraints on microfabric patterns in quartzofeldsphatic
876   mylonites, Ribeira belt (SE Brazil), J. Struct. Geol., 115, 243-262, 2018.

877 Ceccato, A., Menegon, L., Pennacchioni, G., Morales, L.F.G.: Myrmekite and strain
878   weakening in granitoid mylonites, Solid Earth, 9, 1399-1419, 2018.
879 Ceccato, A., Goncalves, P., Pennacchioni, G.: Temperature, fluid content and rheology
880   of localized ductile shear zones in subsolidus cooling plutons, J. Metamorph. Geol.,
881   38, 881-903, 2020.
882 Chen, I.W., Argon, A.S.: Grain boundary and interphase boundary sliding in power law
883   creep, Acta Metallurgica, 27, 749-754, 1979.
884 Chen, K., Scales, M., Kyriakides, S.: Ductile Failure Under Combined Tension and Shear,
885   Journal of Physics: Conference Series, 1063, 2018.
886 Cheng, X., Cao, S., Li, J., Yu, Z., Dong, Y., Lv, M., Liu, J.: Metamorphic, deformation,
887   fluids and geological significance of low-temperature retrograde mylonites of
888   Diancangshan metamorphic massif along Ailaoshan-Red River strike-slip fault zone,
889   Yunnan, China, Sci. China-Earth Sci., 61, 1023-1041, 2018.
890 Chiu, Y.P., Yeh, M.W., Wu, K.H., Lee, T.Y., Lo, C.H., Chung, S.L., Iizuka, Y.: Transition
891   from extrusion to flow tectonism around the Eastern Himalaya syntaxis, Geol. Soc.
892   Am. Bull., 130, 1675-1696, 2018.
893 Collettini, C., Niemeijer, A., Viti, C., Marone, C.: Fault zone fabric and fault weakness,
894   Nature, 462, 907-910, 2009.
895 Cunningham, W.D., Mann, P.: Tectonics of strike-slip restraining and releasing bends,
896   Geological Society, London, Special Publications, 290, 1-12, 2007.
897 Czaplińska, D., Piazolo, S., Zibra, I.: The influence of phase and grain size distribution
898   on the dynamics of strain localization in polymineralic rocks, J. Struct. Geol., 72, 15-
899   32, 2015.
900 Dang, J., Zhou, Y., Rybacki, E., He, C., Dresen, G.: An experimental study on the brittle–
901   plastic transition during deformation of granite, J. Asian Earth Sci., 139, 30-39, 2017.
902 Dayem, K.E., Houseman, G.A., Molnar, P.: Localization of shear along a lithospheric
903   strength discontinuity: Application of a continuous deformation model to the
904   boundary between Tibet and the Tarim Basin, Tectonics, 28, n/a-n/a, 2009.
905 Dong, Y., Cao, S., Cheng, X., Liu, J., Cao, H.: Grain-size reduction of feldspar and flow
906   of deformed granites within the Gaoligong shear zone, southwestern Yunnan, China,
907   Sci. China-Earth Sci., 62, 1379-1398, 2019.
908 Dong, Y., Cao, S., Neubauer, F., Wang, H., Li, W., Genser, J.: Exhumation of the crustal-
909   scale Gaoligong strike-slip shear belt in Southeast Asia, J. Geol. Soc., 2021.
910 Drury, M.R., Humphreys, F.J.: Microstructural shear criteria associated with grain-
911   boundary sliding during ductile deformation, J. Struct. Geol., 10, 83-89, 1988.
912 Egydio-Silva, M., Vauchez, A., Bascou, J., Hippertt, J.: High-temperature deformation
913   in the Neoproterozoic transpressional Ribeira belt, southeast Brazil, Tectonophysics,
914   352, 203-224, 2002.

915   Evans, D.M.: Kabanga magmatic nickel sulphide deposits, Tanzania: morphology and
916   geochemistry of associated intrusions, J. Afr. Earth Sci., 30, 651-674, 2000.

917   Fagereng, A., Beall, A.: Is complex fault zone behaviour a reflection of rheological
918   heterogeneity, Philos Trans A Math Phys Eng Sci 379, 20190421, 2021.

919   Faulkner, D.R., Rutter, E.H.: Can the maintenance of overpressured fluids in large strike-
920   slip fault zones explain their apparent weakness, Geology, 29, 2001.

921   Finch, M.A., Weinberg, R.F., Hunter, N.J.R.: Water loss and the origin of thick
922   ultramylonites, Geology, 44, 599-602, 2016.

923   Fliervoet, T.F., White, S.H., Drury, M.R.: Evidence for dominant grain-boundary sliding
924   deformation in greenschist- and amphibolite-grade polymineralic ultramylonites
925   from the Redbank Deformed Zone, Central Australia, J. Struct. Geol., 19, 1495-1520,
926   1997.

927   Fossen, H., Cavalcante, G.C.G.: Shear zones–A review, Earth-Sci. Rev., 171, 434-455,
928   2017.

929   Franěk, J., Schulmann, K., Lexa, O.: Kinematic and rheological model of exhumation of
930   high pressure granulites in the Variscan orogenic root: example of the Blanský les
931   granulite, Bohemian Massif, Czech Republic, Mineral. Petrol., 86, 253-276, 2006.

932   Frost, E., Dolan, J., Ratschbacher, L., Hacker, B., Seward, G.: Direct observation of fault
933   zone structure at the brittle-ductile transition along the Salzach-Ennstal-Mariazell-
934   Puchberg fault system, Austrian Alps, J. Geophys. Res., 116, 2011.

935   Fusseis, F., Regenauer-Lieb, K., Liu, J., Hough, R.M., De Carlo, F.: Creep cavitation can
936   establish a dynamic granular fluid pump in ductile shear zones, Nature, 459, 974-
937   977, 2009.

938   Ganade de Araujo, C.E., Weinberg, R.F., Cordani, U.G.: Extruding the Borborema
939   Province (NE-Brazil): a two-stage Neoproterozoic collision process, Terr. Nova, 26,
940   157-168, 2014.

941   Gandais, M., Willaime, C.: Mechanical Properties of Feldspars, Feldspars and
942   Feldspathoids: Structures, Properties and Occurrences, 1st ed. Springer, Netherland,
943   pp. 207-246, 1984.

944   Gibert, B., Mainprice, D.: Effect of crystal preferred orientations on the thermal
945   diffusivity of quartz polycrystalline aggregates at high temperature, Tectonophysics,
946   465, 150-163, 2009.

947   Gower, R.J.W., Simpson, C.: Phase boundary mobility in naturally deformed, high-grade
948   quartzofeldspathic rocks: evidence for diffusional creep, J. Struct. Geol., 14, 301-
949   313, 1992.

950   Handy, M.R.: Deformation regimes and the rheological evolution of fault zones in the
951   lithosphere: the effects of pressure, temperature, grain size and time, Tectonophysics,
952   163, 119-152, 1989.

953 Hanmer, S.: Great Slave Lake Shear Zone, Canadian Shield: reconstructed vertical
954   profile of a crustal-scale fault zone, Tectonophysics, 149, 245-264, 1988.

955 Hansen, L.N., Cheadle, M.J., John, B.E., Swapp, S.M., Dick, H.J.B., Tucholke, B.E.,
956   Tivey, M.A.: Mylonitic deformation at the Kane oceanic core complex: Implications
957   for the rheological behavior of oceanic detachment faults, Geochem. Geophys.
958   Geosyst., 14, 3085-3108, 2013.

959 Heidelbach, F., Post, A., Tullis, J.: Crystallographic preferred orientation in albite
960   samples deformed experimentally by dislocation and solution precipitation creep, J.
961   Struct. Geol., 22, 1649-1661, 2000.

962 Hippertt, J., Rocha, A., Lana, C., Egydio-Silva, M., Takeshita, T.: Quartz plastic
963   segregation and ribbon development in high-grade striped gneisses, J. Struct. Geol.,
964   23, 67-80, 2001.

965 Hippertt, J.F.: Breakdown of feldspar, volume gain and lateral mass transfer during
966   mylonitization of granitoid in a low metamorphic grade shear zone, J. Struct. Geol.,
967   20, 175-193, 1998.

968 Hirth, G., Teyssier, C., Dunlap, J.W.: An evaluation of quartzite flow laws based on
969   comparisons between experimentally and naturally deformed rocks, Int. J. Earth Sci.,
970   90, 77-87, 2001.

971 Hirth, G., Tullis, J.: Dislocation creep regimes in quartz aggregates, J. Struct. Geol., 14,
972   145-159, 1992.

973 Hobbs, B.: The Geological Significance of Microfabric Analysis, Preferred Orientation
974   in Deformed Metals and Rocks: An Introduciton to Modern Texture Analysis, pp.
975   463-484, 1985.

976 Holland, T., Blundy, J.: Non-ideal interactions in calcic amphiboles and their bearing on
977   amphibole-plagioclase thermometry, Contrib. Mineral. Petrol., 116, 433-447, 1994.

978 Hollister, L.S., Grissom, G.C., Peters, E.K., Stowell, H.H., Gisson, V.B.: Confirmation
979   of the empirical correlation of Al in hornblende with pressure of solidification of
980   calc-alkaline plutons, Am. Miner., 72, 231-239, 1987.

981 Holyoke, C.W., Tullis, J.: Formation and maintenance of shear zones, Geology, 34, 2006.

982 Imber, I., Holdsworth, R.E., Butler, C.A., Lloyd, G.E.: Fault-zone weakening processes
983   along the reactivated Outer Hebrides Fault Zone, Scotland, J. Geol. Soc., 154, 105-
984   109, 1997.

985 Ishii, K., Kanagawa, K., Shigematsu, N., Okudaira, T.: High ductility of K-feldspar and
986   development of granitic banded ultramylonite in the Ryoke metamorphic belt, SW
987   Japan, J. Struct. Geol., 29, 1083-1098, 2007.

988 Luan, F.C., Paterson, M.S.: Preparation and deformation of synthetic aggregates of
989   quartz, J. Geophys. Res 97, 301-320, 1992.

990 Ji, J., Zhong, D., Sang, H., Zhang, L.: The western boundary of extrusion blocks in the

991   southeastern Tibetan Plateau, Chin. Sci. Bull., 876-881, 2000a.

992   Ji, J., Zhong, D., Shang, H., Qiu, J., Hu, S.: Dating of two metamorphic events on the
993   basalt granulite from Nabang area on the border of China and Burma, Acta Petrol.
994   Sin., 16, 227-232, 2000b.

995   Kilian, R., Heilbronner, R., Stünitz, H.: Quartz grain size reduction in a granitoid rock
996   and the transition from dislocation to diffusion creep, J. Struct. Geol., 33, 1265-1284,
997   2011.

998   Kohlstedt, D.: The Role of Water in High-Temperature Rock Deformation, Reviews in
999   Mineralogy & Geochemistry, Mineralogical Society of America, Washington, D.C.,
1000   pp. 377-396, 2006.

1001 Kronenberg, A.K.: Hydrogen speciation and chemical weakening of quartz, Reviews in
1002   Mineralogy, 29, 123-176, 1994.

1003 Kruhl, J.H.: Preferred lattice orientations of plagioclase from amphibolite and
1004   greenschist facies rocks near the lnsubric Line (Western Alps), Tectonophysics, 135,
1005   233-242, 1987.

1006 Kruse, R., StuÈnitz, H., Kunze, K.: Dynamic recrystallization processes in plagioclase
1007   porphyroclasts, J. Struct. Geol., 23, 1781-1802, 2001.

1008 Langdon, T.G.: Grain boundary sliding revisited: Developments in sliding over four
1009   decades, J. Mater. Sci., 41, 597-609, 2006.

1010 Liu, J.L.: Strain localization and strain weakening in the continental middle crust, Acta
1011   Petrol. Sin., 33, 1653-1666, 2017.

1012 Liu, Z., Ji, J., Sa, X., Chen, Y., Zhong, D.: Crustal deformation and tectonic levels of
1013   Nujiang Gorge since the Miocene, Sci. China-Earth Sci., 61, 93-108, 2017.

1014 Mainprice, D., Bouchez, J.-L., Blumenfeld, P., Tubiâ, J.M.: Dominant c slip in naturally
1015   deformed quartz: Implications for dramatic plastic softening at high temperature,
1016   Geology, 14, 819-822, 1986.

1017 Mancktelow, N.S.: Finite-element modelling of shear zone development in viscoelastic
1018   materials and its implications for localisation of partial melting, J. Struct. Geol., 24,
1019   1045-1053, 2002.

1020 Mancktelow, N.S.: Tectonic pressure: Theoretical concepts and modelled examples,
1021   Lithos, 103, 149-177, 2008.

1022 Mancktelow, N.S., Pennacchioni, G.: The influence of grain boundary fluids on the
1023   microstructure of quartz-feldspar mylonites, J. Struct. Geol., 26, 47-69, 2004.

1024 Mancktelow, N.S., Pennacchioni, G.: The control of precursor brittle fracture and fluid–
1025   rock interaction on the development of single and paired ductile shear zones, J. Struct.
1026   Geol., 27, 645-661, 2005.

1027 Mancktelow, N.S., Pennacchioni, G.: Late magmatic healed fractures in granitoids and
1028   their influence on subsequent solid-state deformation, J. Struct. Geol., 57, 81-96,

1029   2013.

1030   Mancktelow, N.S., Pennacchioni, G.: Intermittent fracturing in the middle continental
1031   crust as evidence for transient switching of principal stress axes associated with the
1032   subduction zone earthquake cycle, Geology, 48, 1072-1076, 2020.

1033   Mansard, N., Raimbourg, H., Augier, R., Précigout, J., Le Breton, N.: Large-scale strain
1034   localization induced by phase nucleation in mid-crustal granitoids of the south
1035   Armorican massif, Tectonophysics, 745, 46-65, 2018.

1036   Martelat, J.-E., Schulmann, K., Lardeaux, J.-M., Nicollet, C., Cardon, H.: Granulite
1037   microfabrics and deformation mechanisms in southern Madagascar, J. Struct. Geol.,
1038   21, 671-687, 1999.

1039   Menegon, L., Pennacchioni, G.: Local shear zone pattern and bulk deformation in the
1040   Gran Paradiso metagranite (NW Italian Alps), Int. J. Earth Sci., 99, 1805-1825, 2009.

1041   Menegon, L., Pennacchioni, G., Malaspina, N., Harris, K., Wood, E.: Earthquakes as
1042   Precursors of Ductile Shear Zones in the Dry and Strong Lower Crust, Geochem.
1043   Geophys. Geosyst., 18, 4356-4374, 2017.

1044   Menegon, L., Pennacchioni, G., Spiess, R.: Dissolution-precipitation creep of K-feldspar
1045   in mid-crustal granite mylonites, J. Struct. Geol., 30, 565-579, 2008.

1046   Miranda, E.A., Hirth, G., John, B.E.: Microstructural evidence for the transition from
1047   dislocation creep to dislocation-accommodated grain boundary sliding in naturally
1048   deformed plagioclase, J. Struct. Geol., 92, 30-45, 2016.

1049   Misra, S., Mandal, N.: Localization of plastic zones in rocks around rigid inclusions:
1050   Insights from experimental and theoretical models, J. Geophys. Res., 112, 2007.

1051   Montardi, Y., Mainprice, D.: A transmission electron microscopic study of the natural
1052   plastic deformation of calcific plagioclases (AN-68-70), Bulletin De Mineralogie,
1053   110, 1-14, 1987.

1054   Morley, C.K.: Variations in Late Cenozoic–Recent strike-slip and oblique-extensional
1055   geometries, within Indochina: The influence of pre-existing fabrics, J. Struct. Geol.,
1056   29, 36-58, 2007.

1057   Morrow, C., Solum, J., Tembe, S., Lockner, D., Wong, T.F.: Using drill cutting separates
1058   to estimate the strength of narrow shear zones at SAFOD, Geophys. Res. Lett., 34,
1059   2007.

1060   Nevitt, J.M., Pollard, D.D.: Impacts of off-fault plasticity on fault slip and interaction at
1061   the base of the seismogenic zone, Geophys. Res. Lett.,, 2017.

1062   Nevitt, J.M., Warren, J.M., Pollard, D.D.: Testing constitutive equations for brittle-
1063   ductile deformation associated with faulting in granitic rock, J. Geophys. Res.,: Solid
1064   Earth 122, 6269-6293, 2017.

1065   Oliot, E., Goncalves, P., Marquer, D.: Role of plagioclase and reaction softening in a
1066   metagranite shear zone at mid-crustal conditions (Gotthard Massif, Swiss Central

1067   Alps), J. Metamorph. Geol., 28, 849-871, 2010.

1068   Oliot, E., Goncalves, P., Schulmann, K., Marquer, D., Lexa, O.: Mid-crustal shear zone

1069   formation in granitic rocks: Constraints from quantitative textural and

1070   crystallographic preferred orientations analyses, Tectonophysics, 612-613, 63-80,

1071   2014.

1072   Olsen, T.S., Kohlstedt, D.L.: Analysis of Dislocations in Some Naturally Deformed

1073   Plagioclase Feldspars, Phys. Chem. Miner., 11, 153-160, 1984.

1074   Olsen, T.S., Kohlstedt, D.L.: Natural deformation and recrystallization of some

1075   intermediate plagioclase feldspars, Tectonophysics, 111, 107-131, 1985.

1076   Oriolo, S., Wemmer, K., Oyhantçabal, P., Fossen, H., Schulz, B., Siegesmund, S.:

1077   Geochronology of shear zones – A review, Earth-Sci. Rev., 185, 665-683, 2018.

1078   Otani, M., Wallis, S.: Quartz lattice preferred orientation patterns and static

1079   recrystallization: Natural examples from the Ryoke belt, Japan, Geology, 34, 2006.

1080   Passchier, C.W., Trouw, R.A.J.: Microtectonics, 2nd ed, Springer, Berlin, 2005.

1081   Pennacchioni, G.: Control of the geometry of precursor brittle structures on the type of

1082   ductile shear zone in the Adamello tonalites, Southern Alps (Italy), J. Struct. Geol.,

1083   27, 627-644, 2005.

1084   Pennacchioni, G., Mancktelow, N.S.: Small-scale ductile shear zones: Neither extending,

1085   nor thickening, nor narrowing, Earth-Sci. Rev., 184, 1-12, 2018.

1086   Pennacchioni, G., Zucchi, E.: High temperature fracturing and ductile deformation

1087   during cooling of a pluton: The Lake Edison granodiorite (Sierra Nevada batholith,

1088   California), J. Struct. Geol., 50, 54-81, 2013.

1089   Platt, J.P.: Rheology of two-phase systems: A microphysical and observational approach,

1090   J. Struct. Geol., 77, 213-227, 2015.

1091   Popp, R.K., Virgo, D., Yoder, H.S., Hoering, T.C., Phillips, M.W.: An experimental study

1092   of phase equilibria and Fe oxy-component in kaersutitic amphibole: Implications for

1093   the f_{H2} and a_{H20} in the upper mantle, Am. Miner., 80, 534-548, 1995.

1094   Precigout, J., Prigent, C., Palasse, L., Pochon, A.: Water pumping in mantle shear zones,

1095   Nat. Commun., 8, 15736, 2017.

1096   Précigout, J., Stünitz, H.: Evidence of phase nucleation during olivine diffusion creep: A

1097   new perspective for mantle strain localisation, Earth Planet. Sci. Lett., 455, 94-105,

1098   2016.

1099   Ratschbacher, L., Merle, O., Davy, P. and Cobbold, P.: Lateral extrusion in the Eastern

1100   Alps, Part 1: Boundary conditions and experiments scaled for gravity, Tectonics, 10,

1101   245-256, 1991.

1102   Ridolfi, F., Renzulli, A.: Calcic amphiboles in calc-alkaline and alkaline magmas:

1103   thermobarometric and chemometric empirical equations valid up to 1,130°C and

1104   2.2 GPa, Contrib. Mineral. Petrol., 163, 877-895, 2011.

Rosenberg, C.L.: Shear zones and magma ascent: A model based on a review of the Tertiary magmatism in the Alps, Tectonics, 23, n/a-n/a, 2004.

Schmid, S.M., Casey, M.: Complete fabric analysis of some commonly observed quartz C-axis patterns, Mineral and Rock Deformation: Laboratory Studies, pp. 263-286, 1986.

Schmid, S.M., Pfiffner, O.A., Froitzheim, N., Schönborn, G., Kissling, E.: Geophysical-geological transect and tectonic evolution of the Swiss-Italian Alps, Tectonics, 15, 1036-1064, 1996.

Schmidt, M.W.: Amphibole composition in tonalite as a function of pressure: an experimental calibration of the Al-in-hornblende barometer, Contrib. Mineral. Petrol., 110, 304-310, 1992.

Scholz, C.H.: Shear heating and the state of stress on faults, J. Geophys. Res.-Solid Earth, 85, 6174-6184, 1980.

Scholz, C.H.: Mechanics of faulting, Annu. Rev. Earth Planet. Sci., 17, 309-334, 1989.

Searle, M.P., Yeh, M.W., Lin, T.H., Chung, S.L.: Structural constraints on the timing of left-lateral shear along the Red River shear zone in the Ailao Shan and Diancang Shan Ranges, Yunnan, SW China, Geosphere, 6, 316-338, 2010.

Sibson, R.H.: Fault rocks and fault mechanisms, J. Geol. Soc., 133, 191-213, 1977.

Spruzeniece, L., Piazolo, S.: Strain localization in brittle-ductile shear zones: fluid abundant vs fluid limited conditions (an example from Wyangala area, Australia), Solid Earth, 7, 1399-1446, 2015.

Stein, E., Dietl, C.: Hornblende thermobarometry of granitoids from the Central Odenwald (Germany) and their implications for the geotectonic development of the Odenwald, Mineral. Petrol., 72, 185-207, 2001.

Stipp, M., StuÈnitz, H., Heilbronner, R., Schmid, S.M.: The eastern Tonale fault zone: a 'natural laboratory' for crystal plastic deformation of quartz over a temperature range from 250 to 700 °C, J. Struct. Geol., 24, 1861-1884, 2002.

Stipp, M., Tullis, J.: The recrystallized grain size piezometer for quartz, Geophys. Res. Lett., 30, 2003.

Stünitz, H., Fitz Gerald, J.D., Tullis, J.: Dislocation generation, slip systems, and dynamic recrystallization in experimentally deformed plagioclase single crystals, Tectonophysics, 372, 215-233, 2003.

Stünitz, H., J.D., F.G.: Deformation of granitoids at low metamorphic grade II: Granular flow in albite-rich mylonites, Tectonophysics, 221, 299-324, 1993.

Tang, Y., Wang, D., Liao, S., Wang, B., Yin, F.: Fabrics and 40Ar/39Ar ages of metamorphic rocks in the Gaoligong tectonic belt: Implications for Cenozoic metamorphism and deformation in the SE Tibetan Plateau, J. Asian Earth Sci., 192, 2020.

1143 Tapponnier, P., Molnar, P.: Active faulting and tectonics of China, J. Geophys. Res., 82,
1144   2905-2930, 1977.

1145 Tapponnier, P., Peltzer, G., Armijo, R., Le Dain, A.Y., Cobbold, P.: Propagating extrusion
1146   tectonics in Asia: new insights from simple experiments with plasticine, Geology, 10,
1147   611-616, 1982.

1148 Tapponnier, P., Lacassin, R., Leloup, P.H., Schärer, U., Zhong, D.L., Liu, X.H., Ji, S.C.,
1149   Zhang, L.S., Zhong, J.Y.: The Ailao Shan/Red River metamorphic belt: Tertiary
1150   leftlateral shear between lndochina and South China, Nature, 343, 431-437, 1990.

1151 Tikoff, B., de Saint Blanquat, M.: Transpressional shearing and strike-slip partitioning
1152   in the Late Cretaceous Sierra Nevada magmatic arc, California, Tectonics, 16, 442-
1153   459, 1997.

1154 Toy, V.G., Prior, D.J., Norris, R.J.: Quartz fabrics in the Alpine Fault mylonites: Influence
1155   of pre-existing preferred orientations on fabric development during progressive uplift,
1156   J. Struct. Geol., 30, 602-621, 2008.

1157 Tribe, I.R., D'Lemos, R.S.: Significance of a hiatus in down-temperature fabric
1158   development within syntectonic quartz diorite complexes, Channel Islands, UK, J.
1159   Geol. Soc., 153, 127-138, 1996.

1160 Tullis, J., Wenk, H.R.: Effect of muscovite on the strength and lattice preferred
1161   orientations of experimentally deformed quartz aggregates, Mater. Sci. Eng. A-Struct.
1162   Mater. Prop. Microstruct. Process., 175, 209-220, 1994.

1163 Tullis, J., Yund, R.A.: Transition from cataclastic flow to dislocation creep of feldspar:
1164   Mechanisms and microstructures, Geology, 15, 606-609, 1987.

1165 Tullis, J., Yund, R.A.: Diffusion creep in feldspar aggregates: experimental evidence, J.
1166   Struct. Geol., 13, 987-1000, 1991.

1167 Twiss, R.J.: Static theory of size variations with stress for subgrains and dynamically
1168   recrystallized grains, U.S.G.S, Open-file Report, pp. 665-683, 1980.

1169 Vannucchi, P.: Scaly fabric and slip within fault zones, Geosphere, 15, 342-356, 2019.

1170 Vauchez, A.: Egydio-Silva, M., Babinski, M., Tommasi, A., Uhlein, A., Liu, D.,
1171   Deformation of a pervasively molten middle crust: insights from the neoproterozoic
1172   Ribeira-Araçuaí orogen (SE Brazil), Terr. Nova, 19, 278-286, 2007.

1173 Wang, W., Song, Z., Tang, Y., Chen, X., Liu, J.: The Ailao Shan–Red River shear zone
1174   revisited: Timing and tectonic implications, Geol. Soc. Am. Bull., 132, 1165-1182,
1175   2019.

1176 Wang, Y., Fan, W., Zhang, Y., Peng, T., Chen, X., Xu, Y.: Kinematics and 40Ar/39Ar
1177   geochronology of the Gaoligong and Chongshan shear systems, western Yunnan,
1178   China: Implications for early Oligocene tectonic extrusion of SE Asia,
1179   Tectonophysics, 418, 235-254, 2006.

1180 Wehrens, P., Berger, A., Peters, M., Spillmann, T., Herwegh, M.: Deformation at the

1181   frictional-viscous transition: Evidence for cycles of fluid-assisted embrittlement and
1182   ductile deformation in the granitoid crust, Tectonophysics, 693, 66-84, 2016.
1183   White, S.H., Knipe, R.J.: Transformation- and reaction-enhanced ductility in rocks,
1184   J. Geol. Soc., 135, 513-516, 1978.
1185   Wibberley, C.A.J., Yielding, G., Di Toro, G.: Recent advances in the understanding of
1186   fault zone internal structure: a review, Geological Society, London, Special
1187   Publications, 299, 5-33, 2008.
1188   Wintsch, R.P., Christoffersen, R., Kronenberg, A.K.: Fluid-rock reaction weakening of
1189   fault zones, J. Geophys. Res.-Solid Earth, 100, 13021-13032, 1995.
1190   Wintscha, R.P., Yi, K.: Dissolution and replacement creep: a significant deformation
1191   mechanism in mid-crustal rocks, J. Struct. Geol., 24, 1179-1193, 2002.
1192   Wirth, R., Voll, G.: Cellular intergrowth between quartz and sodium-rich plagioclase
1193   (myrmekite) - an analogue of discontinuous precipitation in metal alloys, J. Mater.
1194   Sci., 22, 1913-1918, 1987.
1195   Wise, D.U., Dunn, D.E., Engelder, J.T., Geiser, P.A., Hatcher, R.D., Kish, S.A., Odom,
1196   A.L., Schamel, S.: Fault-related rocks: Suggestions for terminology, Geology, 12,
1197   391-394, 1984.
1198   Xia, H.R., Liu, J.L.: The crystallographic preferred orientation of quartz and its
1199   applications, Chin. Sci. Bull., 30, 58-70, 2011.
1200   Xu, Y.G., Yang, Q.J., Lan, J.B., Luo, Z.Y., Huang, X.L., Shi, Y.R., Xie, L.W.: Temporal–
1201   spatial distribution and tectonic implications of the batholiths in the Gaoligong–
1202   Tengliang–Yingjiang area, western Yunnan: Constraints from zircon U–Pb ages and
1203   Hf isotopes, J. Asian Earth Sci., 53, 151-175, 2012.
1204   Xu, Z., Wang, Q., Cai, Z., Dong, H., Li, H., Chen, X., Duan, X., Cao, H., Li, J., Burg, J.-
1205   P.: Kinematics of the Tengchong Terrane in SE Tibet from the late Eocene to early
1206   Miocene: Insights from coeval mid-crustal detachments and strike-slip shear zones,
1207   Tectonophysics, 665, 127-148, 2015.
1208   Yamasaki, T., Wright, T.J., Houseman, G.A.: Weak ductile shear zone beneath a major
1209   strike-slip fault: Inferences from earthquake cycle model constrained by geodetic
1210   observations of the western North Anatolian Fault Zone, J. Geophys. Res.-Solid
1211   Earth, 119, 3678-3699, 2014.
1212   Zhang, B., Chai, Z., Yin, C.Y., Huang, W.T., Wang, Y., Zhang, J.J., Wang, X.X., Cao, K.:
1213   Intra-continental transpression and gneiss doming in an obliquely convergent regime
1214   in SE Asia, J. Struct. Geol., 97, 48-70, 2017.
1215   Zhang, B., Zhang, J., Chang, Z., Wang, X., Cai, F., Lai, Q.: The Biluoxueshan
1216   transpressive deformation zone monitored by synkinematic plutons, around the
1217   Eastern Himalayan Syntaxis, Tectonophysics, 574-575, 158-180, 2012a.
1218   Zhang, B., Zhang, J., Zhong, D., Yang, L., Yue, Y., Yan, S.: Polystage deformation of the

1219   Gaoligong metamorphic zone: Structures, 40Ar/39Ar mica ages, and tectonic
1220   implications, J. Struct. Geol., 37, 1-18, 2012b.

1221 Zhang, J., Peng, T., Fan, W., Zhao, G., Dong, X., Gao, J., Peng, B., Wei, C., Xia, X.,
1222   Chen, L., Liang, X.: Petrogenesis of the Early Cretaceous granitoids and its mafic
1223   enclaves in the Northern Tengchong Terrane, southern margin of the Tibetan Plateau
1224   and its tectonic implications, Lithos, 318-319, 283-298, 2018.

1225 Zhu, R.Z., Lai, S.C., Qin, J.F., Zhao, S.W., Wang, J.B.: Late Early-Cretaceous quartz
1226   diorite–granodiorite–monzogranite association from the Gaoligong belt,
1227   southeastern Tibet Plateau: Chemical variations and geodynamic implications,
1228   Lithos, 288-289, 311-325, 2017.

1229